HELSINKI UNIVERSITY OF TECHNOLOGY
Faculty of Information and Natural Sciences

Antti Snicker

Simulation of fast ion physics in tokamak plasmas

Master's thesis submitted in partial fulfilment of the requirements for the degree of Master of Science in Technology in the Degree Programme in Engineering Physics and Mathematics.

Supervisor : Prof. Rainer Salomaa
Instructor : Dr. Seppo Sipilä

Otaniemi, May 15, 2010

AALTO UNIVERSITY
DEPARTMENT OF APPLIED PHYSICS

ABSTRACT OF MASTER'S THESIS

Author:	Antti Snicker
Department:	Department of Applied Physics
Major subject:	Tfy-56 Advanced Energy Systems
Minor subject:	Tfy-
Title:	Simulation of fast ion physics in tokamak plasmas
Title in Finnish:	Nopeiden ionien fysiikan simulointi tokamak-plasmoissa
Chair:	Tfy-56 Advanced Energy Systems
Supervisor:	Prof. Rainer Salomaa
Instructor:	Dr. Seppo Sipilä

Abstract: A tokamak is a device used to confine a hot and dense plasma to allow energy-producing fusion reactions. A large experimental reactor, ITER, is under construction in France in order to investigate the known problems of fusion energy production. Being of unprecedented size, ITER will reveal new features of tokamak physics, and it is essential to understand them in order to guarantee both the safe use of the reactor and maximal fusion energy production in future reactors.

This thesis presents investigations of two problems related to fast ion physics in tokamaks: the validity of the guiding centre approximation, used in fast ion tracing, as compared to full orbit integration, and the effect of magnetic islands, caused by magnetohydrodynamical instabilities, on fast ion transport. The orbit-following Monte Carlo code ASCOT has been enhanced by the above-mentioned capabilities, which have been carefully verified. Applications of the code's new capabilities are presented.

It was found that in the presence of a strong magnetic field ripple, the guiding centre approximation does not satisfactorily describe the fast in power load to the plasma-facing components of ITER. Under weak magnetic field ripple, however, guiding centre approximation and full orbit integration were found to produce very similar simulation results. A static magnetic island near the plasma edge was observed to increase the fast ion power load even with out the magnetic field ripple.

Number of pages: 6+68 **Keywords:** fusion, alpha particle, gyro motion magnetic island, fast ion losses

Department fills
Approved: **Library code:**

Tekijä:	Antti Snicker
Laitos:	Teknillisen fysiikan laitos
Pääaine:	Tfy-56 Energiatieteet
Sivuaine:	Tfy-

Työn nimi:	Nopeiden ionien fysiikan simulointi tokamak-plasmoissa
Title in English:	Simulation of fast ion physics in tokamak plasmas
Professuuri:	Tfy-56 Energiatieteet
Työn valvoja:	Prof. Rainer Salomaa
Työn ohjaaja:	TkT. Seppo Sipilä

Tiivistelmä:

Tokamak on laite, jonka avulla voidaan pitää koossa kuumaa, tiheää plasmaa ja näin mahdollistaa energiaa tuottavat fuusioreaktiot. Fuusioenergian ongelmia ratkomaan on Ranskaan rakenteilla ITER-koereaktori. Sen tarkoitus on osoittaa fuusioenergian teknistieteellinen toteutettavuus. ITER tuo suuren kokonsa myötä tokamak-fysiikkaan uusia piirteitä, joiden ymmärtäminen on erittäin tärkeää reaktorin turvallisen käytön sekä fuusioenergian tuotannon kannalta.

Tässä työssä keskitytään tutkimaan i) nopeiden hiukkasten seurantaan käytetyn johtokeskusapproksimaation pätevyyttä verrattuna hiukkasten täyden gyroliikkeen mallintamiseen ja ii) magnetohydrodynaamisten epästabilisuuksien aiheuttamien magneettisten saarekkeiden vaikutusta nopeiden hiukkasten kulkeutumiseen. Hiukkasten seurantaan on käytetty ASCOT-ohjelmistoa, jota tässä työssä on laajennettu yllä mainittujen asioiden tutkimiseen. Kunkin ominaispiirteen tutkimiseen käytettyjen matemaattisten mallien esittelyn jälkeen mallit varmistetaan oikeellisiksi erilaisilla testeillä. Malleille esitetään sovelluskohteita, joista osa on toteutettu ja esitetty tuloksineen, osa puolestaan jätetty tutkittavaksi tulevaisuudessa.

Tärkeimpinä tutkimustuloksina todettakoon, että voimakkaan magneettisen kareen läsnäollessa johtokeskusapproksimaatio ei ole riittävän tarkka nopeiden hiukkasten ensiseinään aiheuttaman tehokuorman selvittämiseksi. Sen sijaan pienemmän magneettisen kareen ollessa kyseessä sekä johtokeskusapproksimaatio että täyden gyroliikkeen ratkaiseminen antavat yhtenevät simulaatiotulokset. Hyvin lähellä plasman reunaa sijaitsevan staattisen magneettisen saarekkeen havaittiin lisäävän nopeiden hiukkasten ensiseinämään kohdistuvia häviöitä jopa ilman magneettista rippeliä.

Sivumäärä: 6+68	**Avainsanat:** fuusio, alfa-hiukkanen, gyroliike, magneettiset saarekkeet, nopeiden ionien häviöt
Täytetään osastolla	
Hyväksytty:	**Kirjasto:**

Foreword

This work has been carried out in the Fusion and Plasma Physics group of Aalto University School of Science and Technology as part of the research activities of Association Euratom-Tekes.

Firstly, I would like to thank my instructor Dr. Seppo Sipilä for his invaluable help throughout the work. Without his contribution, you probably could not understand a single sentence. The subject of this thesis was proposed by Docent Taina Kurki-Suonio, who deserves a humble thank-you for the hard work she has been doing in providing great opportunities for young and inexperienced students, like me. For the economical resources I owe to Taina and Academy of Finland. Prof. Rainer Salomaa has been a kind and fair boss along the way. The ASCOT group has been a nice close-knit community for doing science and having some fun, thank you all. Outside our group, I warmly thank to Dr. Emanuele Poli from the Max-Planck-Institut für Plasmaphysik for his kind help.

I would especially like to thank my fiancée Eeva. She has been my tower of strength in the recent years. Without my parents' and family's support I would never have had an opportunity to do science. Words cannot express my gratitude to them.

Last but not least, I want to thank my friends, in particular Erno and Juha - two lifelong, priceless friends.

Otaniemi, May 15, 2010

Antti Snicker

Contents

Chapter 1

Introduction

Mankind has come to an era where the future of energy production is not guaranteed any more. The dramatic climate change has been a hot topic for years, and as a side effect energy issues have obtained a lot of media attention. The undisputed fact is that to ensure the present well-being in the future, we need a lot of cheap, renewable, emission free energy. Another fact is that a limited number of possibilities exists for such an energy source. As a conclusion, mankind should investigate every option from top to bottom, to assess their potential. One suggested future energy source is thermonuclear magnetic fusion [1–3]. Enormous efforts have already been made to prove the feasibility of fusion as an energy source, but a lot of work remains to be done. Small steps taken all over the world are at the very moment joined into a giant step towards commercial fusion power, as a collaboration project common to half of mankind: ITER [4]. The main goal of ITER is to demonstrate that magnetic confinement fusion in a tokamak is scientifically and technologically feasible. ITER will not produce electricity even though it is designed to produce 10 times as much energy as it uses for plasma heating and other things. On the way to commercial fusion, ITER is just one step. After ITER, a DEMO design of a fusion power plant is expected to be built. In DEMO, the main upgrade from ITER is the production of electricity from the heat produced by fusion. After successful operation of DEMO, it is time to build commercial fusion plants.

International collaboration has been the way to fusion energy since the research of the safe use of nuclear fusion became public in the 60's [5]. Information of progress made on one side of the globe quickly reaches the other side. The fusion research in Finland is led by Association Euratom-Tekes. One of

the focuses of the research has been the plasma edge of the tokamak. In the interface between the plasma and the vacuum vessel of a tokamak lie many of the unsolved problems of magnetic confinement fusion. Hence, this topic is of high importance for ITER, and DEMO as well. The fusion and plasma physics research group of the Department of Applied Physics at Helsinki University of Technology, now a part of Aalto university, has focused on simulations of fast ions in tokamak plasmas using the orbit-tracing guiding centre code ASCOT. Special attention has been paid to the simulations of the power load caused by fast ions on ITER plasma-facing components. This thesis consists of enhancements made to the ASCOT simulation model of fast ions. The model has been recently enhanced to include several important effects such as an anomalous diffusion constant arising from microturbulence [6] and a realistic neutral beam injection (NBI) module. It still does not, however, take into account the influence of magnetohydrodynamic (MHD) instabilities that are present in the tokamak plasmas. These instabilities may cause trouble in burning plasmas. Should they appear in the plasma, the confinement will deteriorate, leading to larger fast ion losses and decreased plasma heating.

Moreover, as the Larmor radius of the fast ions becomes comparable to the gradient length of the experiment, the guiding centre approximation used in ASCOT fails [7–9]. This can happen, e.g., in ITER since the magnetic field ripple introduces a toroidal gradient to the field. If the ripple is not compensated, the gradient length may be close to the Larmor radius of the fastest ions, i.e. fusion born 3.5 MeV alpha particles. Until now, such effects of the finite Larmor radius on the transport of the ions have been neglected in ASCOT simulations. The backbone of this thesis consists of two improvements. First, a numerical model for an MHD instability called the neoclassical tearing mode (NTM) [10, 11] is implemented in ASCOT. More subtle instabilities, such as Alfvén eigenmodes (AE) [12, 13], are discussed as well. A magnetic island structure [14] is introduced into the numerical model. Second, the finite Larmor radius effects are taken into account by developing a full orbit integration scheme. In this thesis, the mathematical models for the enhancements are presented and the models are validated. After validating the models, applications are introduced for both models and some of them are studied in more detail by ASCOT simulations.

The structure of this thesis is as follows. In Chapter 2 a short review is

presented on the basics of fusion, tokamak and charged particle motion. The numerical model for full orbit integration is presented in Chapter 3. The applications of full orbit integration are described in Chapter 4. The numerical model for magnetic islands is discussed in theory in Chapter 5 and on the application level in Chapter 6. The conclusions of the thesis and a list of future tasks are discussed in Chapter 7.

Chapter 2

Fusion, the tokamak and charged particle motion

In this Chapter, a short introduction is given to the features and terminology of fusion energy production and plasma physics that are most relevant to the present work. Special attention is paid to the phenomena related to fast ion physics. For readers with no previous knowledge of plasma physics, a more detailed description can be found in Refs. [15, 16]. As this thesis will discuss magnetic confinement fusion in tokamaks, the introduction will focus on tokamak fusion energy production. An introduction to inertial confinement fusion by high intensity lasers can be found in Ref. [17], while magnetic confinement fusion by stellarators is discussed in Ref. [18].

2.1 Energy production in a fusion power plant

The basis of all nuclear energy production, i.e. fission and fusion, is the release of the binding energy of nuclei [19]. A nucleus is lighter than the mass of its constituents, and the difference in terms of energy ($E = mc^2$) is called the binding energy

$$B = \left(\mathrm{Z}m_p + \mathrm{N}m_n - m_{\mathrm{nuc}}\right)c^2, \tag{2.1}$$

where Z is the number of protons and N the number of neutrons in the nuclei, m_p/m_n the proton/neutron mass and m_{nuc} the mass of the nucleus. Nuclear binding energy can be released by two different processes. In fission, one large nucleus is split in two or more daughter nuclei. In the process typically around

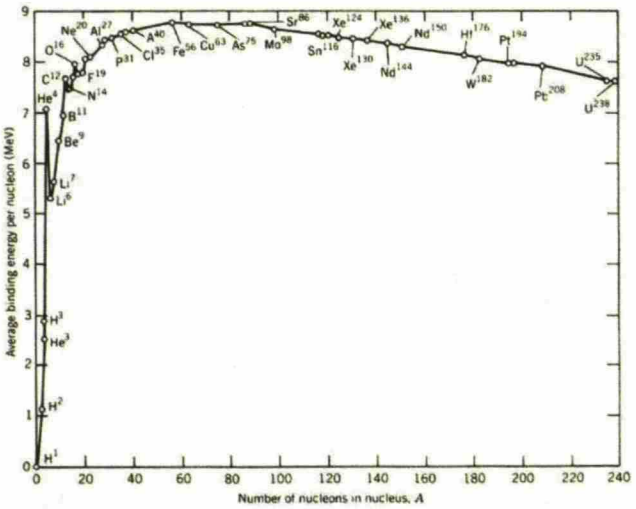

Figure 2.1: Binding energy per nucleon as a function of the mass number.

200 MeV of energy is released. The fission process occurs only in very heavy nuclei, even though in principle it could happen for nuclei heavier than iron as Fig. 2.1 shows. In fusion, two light nuclei fuse to form a slightly larger nucleus. Depending on the fusion reaction, typically around 10 MeV of energy per reaction is released. This can happen for nuclei lighter than iron, see Fig. 2.1. However, in order to make fusion reactions occur, the two positively charged nuclei have to be brought close enough to each other. Thus, energy of the order of the Coulomb barrier between the nuclei is needed. As the charges of the fusing nuclei increase, their (kinetic) energy must be increased as well to overcome this barrier.

To obtain a fusion reaction is, in principle, rather simple - bring enough energy to the system, and the kinetic energy of the nuclei overcomes the potential barrier and fusion reactions occur. To be precise, quantum mechanical tunneling effects [20] make fusion reactions possible well before the Coulomb barrier is overcome. Energy production by fusion reactions is not so simple. In fact, it is extremely difficult. The first thing is to pick up a suitable reaction, i.e. a fuel. By far the easiest reaction is the one in which heavy isotopes of hydrogen, tritium (T) and deuterium (D), fuse into helium

$$ {}^{2}_{1}\mathrm{D} + {}^{3}_{1}\mathrm{T} \rightarrow {}^{4}_{2}\mathrm{He} + {}^{1}_{0}\mathrm{n} + 17.9\,\mathrm{MeV}. \tag{2.2} $$

This is referred to as DT fusion. This is the easiest reaction to achieve because the cross-section in the relevant temperature scale is larger for the DT reaction as compared to its competitors.

Next, proper conditions are needed for fusion reactions to occur. In practice, this means that the DT fuel needs to be hot and dense, and kept confined for a sufficiently long period of time [15]. Three different ways to obtain such conditions have been proposed so far: i) magnetic confinement fusion by tokamak or ii) by stellarator and iii) inertial confinement fusion. This thesis deals with the first alternative, where the fuel is kept confined by magnetic fields created by both external field coils and internal plasma currents. In stellarators, the magnetic field is produced by external field coils only, which may help obtaining a steady state operation needed for a fusion power plant. However, at the moment stellarators are one generation behind tokamaks and, therefore, a lot of research is still needed. The last alternative is completely different. The idea behind inertial fusion is not to confine the plasma but rather to obtain for a very short time such a high density that enough fusion reactions occur even without confinement. In inertial confinement fusion, fuel pellets are compressed spherically to high density with laser or x-ray beams. Actually the laser is used to vaporize the outer layer of the pellet. The temperature difference between the core and edge of the pellet will explode the outer layer away and the recoil will then compress the core of the pellet to extremely high density. As the fuel pellet is compressed, the fusion reactions begin. The main difficulties on the way to commercial reactors are the high frequency injection of the pellets needed to produce energy, impurities appearing in the reactor chamber, and the high technological requirements for the lasers [17].

In all of the suggested fusion reactor concepts the actual energy production relies on the help of the neutrons born in the reaction, see Eq. (2.2). As a neutral particles, neutrons are not confined by the magnetic field. They escape the plasma and hit the vessel walls transferring their kinetic energy to the coolant water. The heated water is boiled to steam and the rest is common, well-established technology for all heat power plants. The fuel, i.e. tritium and deuterium, is harvested as follows. Deuterium exists in large enough concentrations in sea water and soil and the resources are practically infinite. Tritium is slightly more difficult: being a radioactive isotope, it decays spontaneously. The idea is to create the tritium inside the reactor in breeding blankets located right

outside the vacuum vessel. There, again, the fusion-born neutrons are utilized via the reactions

$$ {}^{1}_{0}\mathrm{n} + {}^{6}_{3}\mathrm{Li} \rightarrow {}^{3}_{1}\mathrm{T} + {}^{4}_{2}\mathrm{He} + 4.6\ \mathrm{MeV} \tag{2.3} $$

$$ {}^{1}_{0}\mathrm{n} + {}^{7}_{3}\mathrm{Li} \rightarrow {}^{3}_{1}\mathrm{T} + {}^{4}_{2}\mathrm{He} + {}^{1}_{0}\mathrm{n} - 2.5\ \mathrm{MeV}. \tag{2.4} $$

As a result, the fuel actually loaded into the reactor consists of deuterium and lithium. As the tritium is radioactive, the amount of tritium is inventoried carefully. It should also be noted that the neutrons born in the fusion reaction of Eq. (2.2) are extremely important for energy transport and tritium breeding. On the other hand, if one could get rid of the radioactive tritium, the problems with tritium retention to the wall structures [21] could be alleviated.

In summary, there exist almost unlimited fuel reserves, the energy production is very efficient and pollution free, and the only radioactive isotope involved is tritium, which is the fuel, not an end product. The technology is not ready, but the concept is feasible and the potential benefits are huge. Hence, it is reasonable to say that tokamak magnetic confinement fusion is well worth studying.

2.1.1 The tokamak

The tokamak [15] is the most promising magnetic fusion device. It consists of several main components such as magnets, a vacuum vessel, a blanket, divertor plates, diagnostics (mostly in experimental devices), external heating systems and a cryostat. All of these are shown in a technical illustration of ITER in Fig. 2.2. A tokamak's magnetic field is composed of a toroidal component B_ϕ, produced by external poloidal field coils, and a poloidal component B_θ induced by the toroidal plasma current, which in turn is created by the central transformer. These two components form the helical total magnetic field $\vec{B}$. The magnetic field structure consists of essentially two concentric layers. In the inner layer the field lines are closed, and the last closed field line is called the separatrix. In the outer layer, outside the separatrix, the field lines are open. The scrape-off layer (SOL) that separates the confined plasma from the plasma-facing components, is just outside the separatrix and plays a crucial role in phenomena such as plasma recycling, impurity transport and heat transfer [22]. Another important component are the external heating systems, such as the neutral beam injection (NBI) system [23]. The idea behind NBI is extremely simple - the ions

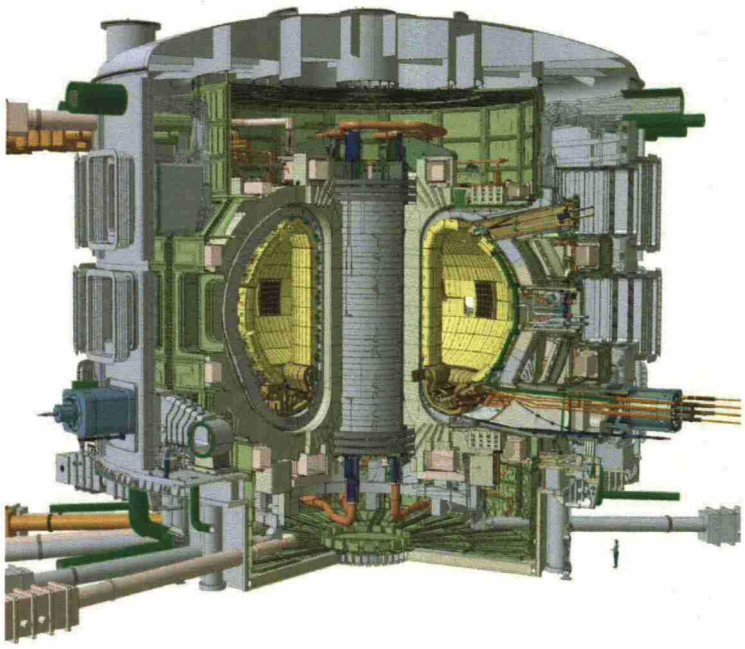

Figure 2.2: ITER, the world's largest tokamak (under construction in Cadarache, France) with a height of 29 meters and a diameter of 28 meters. ©ITER organization

are accelerated to high energy (1 MeV in ITER), neutralized and injected into the plasma. The neutrals are quickly ionized in the plasma, and then they transfer their kinetic energy to the colder main plasma. The fast NBI-born ions are the major fast ions species in many experimental reactors, such as ASDEX Upgrade. In ITER, fusion born alpha particles will dominate the fast ion physics. Diagnostics reveal important physics in experimental devices. However, due to their detrimental influence on confinement and stability, not forgetting the fact that they diminish the usability of the device by requiring maintenance, and the fact that there is far less use for them in commercial reactors, only very limited number of diagnostics will be installed to power plant tokamaks. However, the diagnostics are an invaluable tool in understanding the plasma behaviour and automatizing the plasma control.

The physics of tokamaks is currently well understood. It seems that magnetic confinement fusion in a tokamak is physically feasible. Hence, the main research interest has moved from basic plasma physics of tokamaks to the tech-

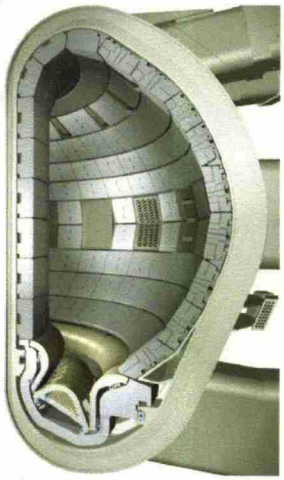

Figure 2.3: Cut-away of the ITER vacuum vessel showing part of the 440 blanket modules attached to the inner wall and the divertor cassettes at the bottom. ©ITER Organization

nological aspects of the tokamak design and how to implement the ideas to actual energy producing devices. One of the main issues is a problematic choice of the plasma-facing components (PFC). Due to the Z^2 dependence of bremsstrahlung [15], small-Z elements are favored, whereas the erosion processes such as chemical and physical sputtering would suggest using a high-Z element [22]. Moreover, tritium retention to carbon is considered to as a major problem for a commercial fusion power plant. In practice, the final choice is often a combination of both low and high Z elements, i.e. carbon, tungsten and beryllium. The whole field of research, plasma surface interaction or PSI, is devoted to solving the material problems in tokamaks. A slice of the ITER vacuum vessel is shown in Fig. 2.3, with the different PFC species illustrated by colors. Yet another problem with the PFC's, which has not been present in earlier tokamaks but will appear in ITER, is the large wall load caused by the bombardment of fast particles [24]. Especially the divertor targets and limiters, see Fig. 2.3, will be under heavy power load. In a commercial reactor the divertor plates cannot be changed very often, so they should endure as long as possible. Otherwise the availability of the power plant is reduced, increasing the final price of the fusion electricity.

2.1.2 Coordinate systems and flux functions

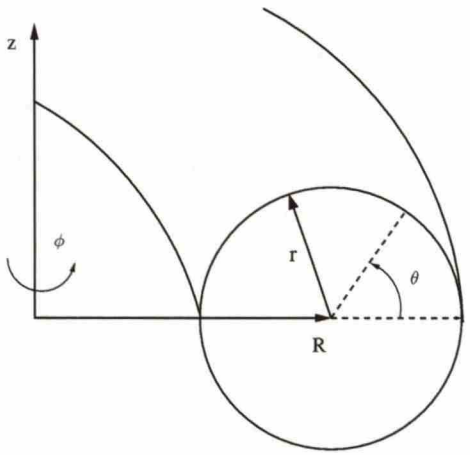

Figure 2.4: A tokamak's cylindrical coordinate system.

Three different coordinate systems are typically used for the tokamaks. The first is the Cartesian coordinate system. The second system, an obvious choice after looking at the geometry of the tokamak, is the cylindrical coordinate system illustrated in Fig. 2.4. The last but not the least is the magnetic coordinate system [25–27]. It is rather difficult to justify which one is the most suitable in general as they all have their pros and cons. It could be said, though, that the Cartesian coordinates are a safe choice because of their general nature. Compared to the Cartesian system, the cylindrical coordinate system offers a very convenient way to illustrate some physical quantities, e.g. the toroidal magnetic field. An especially useful presentation for cases of both circular and non-circular cross section are the (R,ϕ,z) coordinates, which can be considered a more general form of the cylindrical system. The magnetic coordinates, being canonical coordinates of the drift Hamiltonian [28] offer some significant advantages. They provide a natural way to describe a particle moving in a magnetic field. In some cases, they may even simplify the information required to solve the particle trajectories. Magnetic coordinates suffer from a singularity at the separatrix. Hence, the particles that cross the separatrix would cause problems. This is, however, easily avoided by switching to Cartesian or cylindrical coordinates before the problem is encountered.

The usual way to interpret the magnetic coordinates is as follows. In toroidal

symmetry and scalar pressure equilibrium, χ is a constant pressure surface or magnetic flux within this surface, θ_b labels an angle along the pressure surface and ζ is the distance along the field line (to be more precise, $d\zeta/B$ is the differential distance). The magnetic field in this coordinate system can be given in many forms. The covariant form of the field is given by

$$\vec{B} = g\left(\chi_p\right)\nabla\zeta + \mu_0 I\left(\chi_p\right)\nabla\theta + \delta\left(\chi_p, \theta\right)\nabla\chi_p, \tag{2.5}$$

where g, I and δ are functions that generate the magnetic field, χ_P is the poloidal flux and the functions are interpreted as follows. The plasma current flowing through the poloidal cross-section of the plasma is I, g is the coil current, i.e. the current flowing through the toroidal cross-section but only inside the torus, and finally δ is a function that usually does not play a major role but it is closely related to the Pfirsch-Schlüter current [27]. The other commonly used form is the so-called Clebsch representation [28] or contravariant form which is given by

$$\vec{B} = \nabla\psi_p \times \nabla\theta - \nabla\psi_p \times \nabla\zeta. \tag{2.6}$$

This form can be derived from the Euler vector potential

$$\vec{A} = \psi_p\nabla\theta + \nabla\zeta. \tag{2.7}$$

To understand the flux surfaces we assume an axisymmetric plasma equilibrium where the magnetic field lines lie on nested annular toroidal magnetic surfaces. Similarly as in ordinary fluid mechanics, this 2D magnetic configuration can be defined by the flux function χ given by [15]

$$\chi_p = \int B_\theta R\, dr, \tag{2.8}$$

where we have selected to use the poloidal flux. The toroidal flux is defined in a similar manner. This flux function has a couple of important properties. Firstly, it is always constant on magnetic surfaces, i.e.

$$\vec{B} \cdot \nabla\chi = 0. \tag{2.9}$$

Hence, it can be used to label the magnetic surfaces. Secondly, it can be used to

calculate the poloidal magnetic field components. They are given by [15]

$$B_R = -\frac{1}{R}\frac{\partial \chi}{\partial z} \tag{2.10}$$

$$B_z = \frac{1}{R}\frac{\partial \chi}{\partial R} \tag{2.11}$$

Later on the common procedure where the poloidal flux is normalized to span from zero to unity is used, i.e.

$$\chi_n = \frac{\chi - \chi_c}{\chi_s - \chi_c}, \tag{2.12}$$

where χ_c is the poloidal flux at the magnetic axis and χ_s the poloidal flux at the separatrix. It is also common practice to use the flux label ρ defined by

$$\rho = \sqrt{\chi_n}. \tag{2.13}$$

This contains exactly the same information as χ_n, but using ρ has become an established practice in the computational plasma physics community as it behaves like the linear radial coordinate in a purely cylindrical system.

2.2 Motion of a charged particle in an electromagnetic field

The most general way to describe the relativistic charged particle behaviour in an electromagnetic field is given by Newton's second law combined with the Lorentz force [29]

$$\frac{d\vec{p}}{dt} = \frac{d(\gamma m \vec{v})}{dt} = q\left(\vec{E} + \vec{v} \times \vec{B}\right), \tag{2.14}$$

where $\gamma = (1 - v^2/c^2)^{-1/2}$, $\vec{p}$ is the momentum of the particle, $\vec{E}$ is the electric field vector, $\vec{B}$ is the magnetic field vector and $\vec{v}$, q, and m are the velocity, charge, and mass of the particle, respectively. The above relation, namely the cross term $\vec{v} \times \vec{B}$, leads to the situation where the particle gyrates around the magnetic field line. As we saw earlier on, in Section 2.1.1, the magnetic field of the tokamak has a non-trivial structure which complicates the solution of Eq. (2.14). There are two conceptually very different ways to solve this equation. The first is the so-called guiding centre approximation [30] (GCA) and the second is the direct integration of Eq. (2.14), which is from now on called full orbit

integration. There are at least two essential differences worth of mention. First, while the full orbit integration is exact, as long as the numerical methods are exact, the GCA loses the actual location of the particle and is only valid when the magnetic field does not change too much inside one Larmor orbit, i.e.

$$\frac{1}{\Omega B}\frac{dB}{dt} \ll 1 \tag{2.15}$$

and

$$\frac{R_L |\nabla B|}{B} \ll 1, \tag{2.16}$$

where the Ω and R_L are the gyro frequency and Larmor radius of the particle (see the next section regarding GCA). Hence, the validity of Eqs. (2.15) and (2.16) should always be checked for the case being studied, i.e. for the ion species and the magnetic field. Second, the GCA is much faster from the computational point of view. The fast gyration limits the time step that can be used in full orbit integration, making it substantially slower than GCA. One would prefer to use the GCA in tasks that are computationally heavy and do not require knowledge about the accurate position of the ions. Full orbit integration is required when the GCA approximation breaks down or the exact position of the particle is needed to, e.g., compile statistics of the accurate distributions of wall-hitting particles.

2.3 The guiding centre approximation

As mentioned in the previous section, the usual solution for the particle tracing is the guiding centre approximation, where the exact location of the particle is lost by averaging out the fast gyration around the magnetic field line [30]. A new equation of motion, to be used instead of Eq. (2.14), is constructed by the averaging procedure. The justification for this is that the gyration of electrons and ions around the magnetic field line is usually of little interest, whereas the movement of the particle's guiding centre is the essential thing. This is because the radius of the gyration of confined particles usually tends to be of the order of millimeters to centimeters whereas the guiding centre orbits may easily span several meters. Only the radius and the frequency of the gyration, called the Larmor radius R_L and Larmor frequency Ω, are retained in the guiding centre

equations. The expressions for these are

$$R_L = \frac{v_\perp}{\Omega}, \tag{2.17}$$

where the $v_\perp$ is the velocity component perpendicular to the magnetic field vector, and

$$\Omega = \frac{qB}{m}. \tag{2.18}$$

These two quantities define how fast the particle gyrates around the magnetic field line (Ω) and how far the particle is, on the average, from the magnetic field line (R_L).

As was pointed out earlier on, the nontrivial structure of a tokamak's magnetic field, namely its curvature and gradient, makes charged particles undergo drift motion. In other words, particles are not perfectly confined to the magnetic field line. Usually the drifts are divided into three separated parts: the $\vec{E} \times \vec{B}$ drift $\vec{v}_E$ caused by the interplay of the electric and magnetic fields, the curvature drift $\vec{v}_C$ and the gradient drift $\vec{v}_G$ caused by the corresponding features of the magnetic field structure. The forms for these drift velocities are derived, for example, in Ref. [15], and they have the expressions

$$\vec{v}_E = \frac{\vec{E} \times \vec{B}}{B^2}, \tag{2.19}$$

$$\vec{v}_G = \frac{W_\perp}{qB^3} \vec{B} \times \nabla B, \tag{2.20}$$

where $W_\perp = mv_\perp/2$ is the perpendicular energy component, and

$$\vec{v}_C = \frac{2W_\parallel}{qB^4} \left(\vec{B} \times \left(\vec{B} \cdot \nabla \right) \vec{B} \right), \tag{2.21}$$

where $W_\parallel = mv_\parallel/2$ is the parallel energy component. The last two can in some cases be combined together. From Maxwell's equations we have, for the current-free case, $\nabla \times \vec{B} = 0$ and on the other hand $\nabla B^2 = 2B\nabla B$. Now taking the curl of the Maxwell equation we find that

$$0 = \nabla \times \nabla \times \vec{B} = \frac{1}{2} \nabla B^2 - \left(\vec{B} \cdot \nabla \right) \vec{B}, \tag{2.22}$$

which implies that

$$\left(\vec{B}\cdot\nabla\right)\vec{B}/B = \nabla B. \tag{2.23}$$

Hence, the curvature and gradient drifts can be combined to the magnetic drift velocity v_B with the expression

$$\vec{v}_B = \vec{v}_G + \vec{v}_C = \frac{W_\perp + 2W_\parallel}{qB^3}\vec{B}\times\nabla B. \tag{2.24}$$

Now using Eqs. (2.18), (2.19) and (2.24) we find that the total guiding centre velocity has the form

$$\vec{v}_{GC} = \frac{v_\parallel\vec{B}}{B} + \frac{\left(v^2+v_\parallel^2\right)\left(\vec{B}\times\nabla\vec{B}\right)}{2\Omega B^2} + \frac{\vec{E}\times\vec{B}}{B^2}, \tag{2.25}$$

where the first term on the right hand side is the velocity parallel to the magnetic field and the last two are the drift terms discussed above. Often a slightly modified version of Eq. (2.25) is used, derived from the Hamiltonian theory that automatically ensures conservation of the total energy. For more details see Ref. [31].

2.4 ASCOT

The numerical studies in this thesis are made using the guiding centre orbit tracing code ASCOT [32]. The code has been improved by the new models described in the following Chapters. This section reviews the starting point for the improvements. ASCOT is, roughly speaking, composed of three elements: handling of background and other input data, orbit tracing and diagnostics. As a broader view, ASCOT can be regarded as not only a physics code but also an engineering code. It can be used e.g. to evaluate the realistic wall loads caused by fast ions hitting the reactor wall [24]. This demands that the set-up of the code is as realistic as possible. In practice, this means that 3D PFC's and magnetic fields are imported from the experiment databases. Thus the background data is given as arrays of numbers, which need to be accurately interpolated during the simulation. For the fast evaluation of guiding centre traces, the magnetic coordinates are (optionally) used inside the separatrix and the Cartesian coordinates in the region of open field lines. The magnetic coordinate grid is

created from the Cartesian grid, in the preprocessing phase. The beamlet-based NBI module, used to generate the input file for fast NBI-born ions, belongs to the preprocessing phase as well. The model is designed to be as realistic as possible, modeling each beamlet, i.e. a sub-beam, of every NBI positive ion neutral injector (PINI). Recently, it has been benchmarked to the PENCIL code [33]. The plasma properties are given as density and temperature profiles and a radial electric field profile can be imported to the code as well. ASCOT also requires a rather long input file listing the running options such as the coordinate system to be used and the amount of time the particles are to be traced. This, and the initial particle file, are created in the preprocessing phase.

The orbit tracing part is the vital ingredient. The typically numerous guiding centres of ions or electrons are traced in a given magnetic (and electric) field in the chosen coordinate system. The effect of particle interactions with the background plasma by Coulomb collisions are taken into account by Monte Carlo operators derived from the Fokker-Planck equation [34, 35] using Rosenbluth potentials [35, 36]. The collisions affect the particle's pitch $\xi = v_{\parallel}/v$ and energy E. Without time scale acceleration of these interactions, it is necessary to follow particles for a large number of bounce orbits, since the collision times τ_c are of the order of 1 to 10 ms and the bounce time τ_b is of the order of 1 μs. This may lead to excessive CPU time consumption. Hence, an interaction acceleration factor has been introduced to speed up the simulation. Acceleration can be used correctly only for particles on periodic orbits. At the heart of the guiding centre orbit tracing code are the equations of motion. In ASCOT, a canonical Hamiltonian formulation is used to derive proper equations for the guiding centre and its velocity. The procedure of Ref. [31] is used. Again, either coordinate system can be used and therefore two sets of equations of motion are needed. The fastest simulation is obtained by using magnetic coordinates inside the separatrix and changing to the Cartesian system when approaching the plasma boundary.

The last part, i.e. the diagnostics, is essentially the output of the code. Depending on the problem, ASCOT can produce several different distributions, orbits of the ions, or user defined quantities. The output is post-processed with Matlab or some other software to present the output data in graphic form.

To conclude, ASCOT is a versatile computer code with a capability to simulate many aspects of current, and forthcoming, magnetic fusion experiments. It

has been used in numerous studies of charged particle behaviour such as reverse runaway losses during current ramp-up with LH waves [37], ion cyclotron minority ion heating and current drive [38], neoclassical radial current balance in tokamaks and transition to the H mode [39] and divertor and wall load distribution studies [24, 40].

Chapter 3

Numerical model for full orbit integration

As was pointed out earlier on, in the full orbit integration scheme Eq. (2.14), is integrated directly without approximations. The non-relativistic version of this equation, i.e. with $\gamma = 1$, is currently implemented. This holds as long as only ions are being traced. Being light particles, electrons can be relativistic and a relativistic version of the present numerical model should be applied to them. In addition to Eq. (2.14), the definition of the velocity

$$v = \frac{d\vec{x}}{dt} \tag{3.1}$$

is used as well. It is convenient to write Eq. (2.14) in the form

$$\frac{dv}{dt} = \frac{q}{m}\left(\vec{E} + \vec{v} \times \vec{B}\right). \tag{3.2}$$

Then these two equations are solved, numerically, and the exact orbit of the particle is obtained. The system to be solved contains ordinary differential equations. It should be noted, however, that the fields are functions of the position and therefore solving this set of equations is not trivial. Moreover, the magnetic field is usually given as a tabulated array from the experimental database and has to be interpolated during the orbit simulation, which further complicates the problem. The equations can be solved with many different solvers. For our purposes the most important features of the solver are its speed and accuracy.

3.1 Leap-frog Boris method

One way to solve the ordinary differential equation system mentioned above is the leap-frog Boris method [41]. The basic idea in the leapfrog Boris method is that the two variables $\vec{x}$ and $\vec{v}$ are advanced in time alternately. The equations of motion are then simplified by the following approximations

$$d\vec{v} \approx \vec{v}_1 - \vec{v}_0 \tag{3.3}$$

$$dt \approx \delta t \tag{3.4}$$

$$\vec{v} \approx \frac{\vec{v}_1 + \vec{v}_0}{2}. \tag{3.5}$$

The subscript denotes the variables' point in time. Inserting these approximations to Eqs. (2.14) and (3.1) one finds that

$$\frac{\vec{v}_1 - \vec{v}_0}{\delta t} = \frac{q}{m}\left(\vec{E}(\vec{x}_{1/2}) + \frac{\vec{v}_1 + \vec{v}_0}{2} \times \vec{B}(\vec{x}_{1/2})\right) \tag{3.6}$$

$$\frac{\vec{x}_{3/2} - \vec{x}_{1/2}}{\delta t} = \vec{v}_1, \tag{3.7}$$

where the points in time are again defined by the subscripts. For example,

$$\vec{x}_{1/2} = \vec{x}((n + 1/2)\,\delta t) \tag{3.8}$$

$$\vec{v}_1 = \vec{v}((n + 1)\,\delta t), \tag{3.9}$$

where $n = 0, 1, 2\ldots$ with the initial values given with $n = 0$. In the situation of vanishing electric field, $\vec{E} = 0$, it is possible to solve $\vec{v}_1$, or to be precise, $\vec{y} = (\vec{v}_1 + \vec{v}_0)/2$. This is done by first solving $\vec{y}$ implicitly and then taking the cross product with the magnetic field vector

$$\vec{y} = \vec{v}_0 + \frac{\delta t q}{2m}\vec{y} \times \vec{B} \tag{3.10}$$

$$\vec{y} \times \vec{B} = \vec{v}_0 \times \vec{B} + \frac{\delta t q}{2m}\left(\vec{y} \times \vec{B}\right) \times \vec{B}. \tag{3.11}$$

Then one can substitute $\vec{y} \times \vec{B}$ from Eq. (3.11) to Eq. (3.10) to obtain

$$\vec{y} = \vec{v}_0 + \frac{\delta t q}{2m}\vec{v}_0 \times \vec{B} + \left(\frac{\delta t q}{2m}\right)^2 \left(\vec{y} \times \vec{B}\right) \times \vec{B} \tag{3.12}$$

and after simplifying the cross product and moving one term to the left hand side one arrives at

$$\vec{y}\left(1+\left(\frac{\delta tq}{2m}\right)^2\right) = \vec{v}_0 + \frac{\delta tq}{2m}\vec{v}_0 \times \vec{B} + \left(\frac{\delta tq}{2m}\right)^2 \left(\vec{y}\cdot\vec{B}\right)\vec{B}. \tag{3.13}$$

At this stage one needs to approximate the term $(\delta tq/2m)^2\left(\vec{y}\cdot\vec{B}\right)\vec{B}$ in order to solve the unknown $\vec{y}$. Comparing it to the other two terms at the right hand side of the Eq. (3.13) and assuming that δt is small, as it should be, this term is one order of magnitude smaller than the others. Hence, it is justified to approximate $\left(\vec{y}\cdot\vec{B}\right)\vec{B} \approx \left(\vec{v}_0\cdot\vec{B}\right)\vec{B}$. Then it is easy to solve Eq. (3.13) for $\vec{y}$

$$\begin{aligned}\vec{y} &= \frac{\vec{v}_1+\vec{v}_0}{2} \\ &= \frac{\vec{v}_0 + (q\delta t/2m)\left(\vec{v}_0\times\vec{B}_{1/2} + \vec{v}_0\cdot\left(q\delta t\vec{B}_{1/2}/2m\right)\vec{B}_{1/2}\right)}{1+\left(q\delta t\vec{B}_{1/2}/2m\right)^2}.\end{aligned} \tag{3.14}$$

Now it is clear that when $\vec{v}_0$ and $\vec{x}_{1/2}$ are given, Eq. (3.14) gives $\vec{v}_1$ and then Eq. (3.7) is used to obtain $\vec{x}_{3/2}$, finally ending the cycle. With an appropriate choice of δt, the method has been proven very reliable and is widely used in, e.g., particle-in-cell codes [42, 43] to simulate charged particle motion. The fields are computed at the middle of the points where the velocities are calculated. Hence, the forces are calculated at the same time point as the location $\vec{x}$. In the following, the leapfrog Boris method is referred to as method I.

3.2 Implicit Boris method

The difference between the leapfrog and the implicit Boris method, from now on method II, is that in the implicit Boris method the variables $\vec{x}$ and $\vec{v}$ are advanced together. This means that the variables are defined at the same time point, while the fields are again computed at the middle points:

$$\frac{\vec{v}_1-\vec{v}_0}{\delta t} = \frac{q}{m}\left(\vec{E}_{1/2} + \frac{\vec{v}_1+\vec{v}_0}{2}\times\vec{B}_{1/2}\right) \tag{3.15}$$

$$\frac{\vec{x}_1-\vec{x}_0}{\delta t} = \frac{\vec{v}_1+\vec{v}_0}{2}, \tag{3.16}$$

where the fields are given by

$$\vec{E}_{1/2} = \vec{E}\left(\frac{\vec{x}_1 + \vec{x}_0}{2}\right) \tag{3.17}$$

$$\vec{B}_{1/2} = \vec{B}\left(\frac{\vec{x}_1 + \vec{x}_0}{2}\right). \tag{3.18}$$

The fundamental difference between methods I and II is that method II involves evaluation of the fields at an unknown position. Therefore, one must use iterative methods to obtain the new velocity from Eq. (3.15). For the first iteration, one needs an estimate for the new location $\vec{x}_1$ in order to obtain the forces from Eq. (3.17) and Eq. (3.18). Method I gives a good estimate for $\vec{x}_1$. Then an iteration loop is performed to obtain the new velocity from Eq. (3.15) and the new location from Eq. (3.16). If there is no electric field in the system, Eq. (3.14) can again be used to obtain a new velocity. While method I is very easy to implement and use, it sets a limit for the time step and can be inefficient in some cases. Method II, on one hand, provides a more stable scheme over a wide range of time steps, but on the other hand is much more difficult to implement, may involve high CPU cost per time step, and the convergence of linear solvers will deteriorate as δt increases.

3.3 Implementation to ASCOT

The full orbit integration scheme is implemented in ASCOT as an alternative for the guiding centre integration, i.e. a guiding centre time step can be divided into sub-steps advanced in time by the full orbit integrator. The size of the full orbit step is adjusted as follows. The current position and the Larmor frequency are used to deduce the time it takes to complete a single gyro orbit (δt_L), a fixed number is used to divide the gyro orbit into N segments. Then, the full orbit time step is just $\delta t = \delta t_L / N$. After the full orbit solver has completed the whole guiding centre time step, the code returns to the guiding centre location. Thereafter, the work flow continues normally. Currently only the Cartesian version of the equations of motion is implemented. As can be seen from Ref. [34], the collision operator is derived for real particles, not the guiding centre particles. Hence, using the full orbit location of the particle in the calculation of collision frequencies actually improves the accuracy of the collision model.

The full orbit integration extends to the PFC's, since only the magnetic field is needed to trace the gyro orbit and the magnetic background data extends well beyond the PFC's. Near the PFC, the wall hit collision check needs to be done after each and every full orbit time step. While it is very CPU time consuming, it will guarantee the accurate wall hit locations, as shown in Section 4.4.

Chapter 4

Applications of full orbit integration

4.1 Validation of the implementation

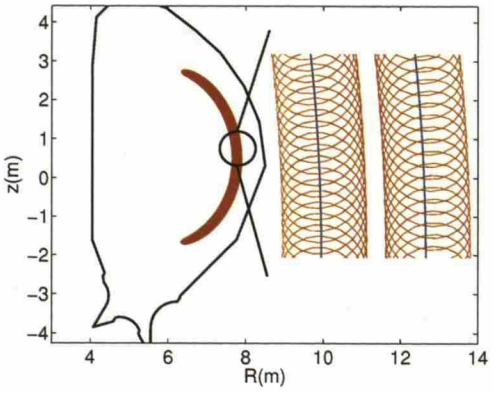

Figure 4.1: Trace of a 3.5 MeV α with an initial pitch angle ξ=-0.376. The magnetic background of ITER discharge #585 was used. The guiding centre is shown in blue and the full orbit in red.

To validate the full orbit integration routine several tests were made. First, the orbit of a fusion-born 3.5 MeV α-particle was calculated both with guiding centre and full orbit integration. The comparison is shown in Fig. 4.1. As the orbits match quite nicely, the full orbit was integrated for around 40 ms or 1650 bounce times and the radial coordinate, see Eq. (2.13), was plotted as a function

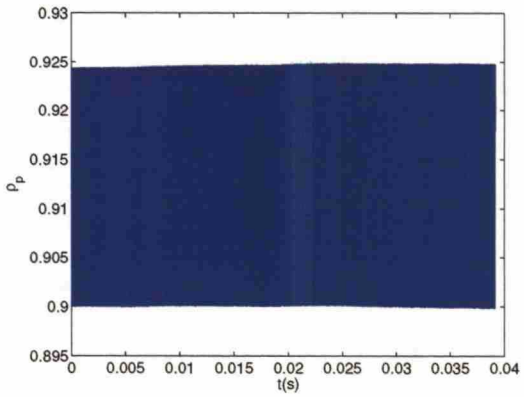

Figure 4.2: The radial coordinate as a function of time in axisymmetric magnetic field of ITER discharge #585.

of time. As the magnetic background was an axisymmetric version of ITER discharge #585, the orbit should stay at the same magnetic flux surface. This is illustrated in Fig. 4.2. The orbit is trapped and spans a finite width (banana width) in the radial coordinate. As can be seen from the figure, the orbit drifts just $\Delta\rho = 0.001$ during 40 ms. When the collisions are turned on, this level of numerical drift is negligible compared to the radial drift caused by the collisions during 40 ms. These results, together with simpler tests not presented here, show that the implementation can be used in full orbit particle tracing. In the next sections, the full orbit solver is applied to physics simulations.

4.2 Full orbit calculation of fusion alpha wall load on ITER

The integer nature of the toroidal field coils cause an effect called magnetic ripple. This inhomogeneity in the background magnetic field makes the magnetic configuration genuinely three-dimensional. The ripple strength is defined by

$$\delta(R,z) = \frac{B_{\max} - B_{\min}}{B_{\max} + B_{\min}}. \tag{4.1}$$

Hence, a large ripple strength corresponds to the situation where the toroidal gradient of the magnetic field is large, and vice versa. The largest value of $\delta(R,z)$ is typically called the ripple strength. In ITER, the toroidal magnetic field is produced by 18 toroidal field coils [44, 45], which is only half the num-

ber of toroidal field coils (32) in JET, currently the largest tokamak in the world. Hence, the large ripple strength, and thus the large inhomogeneity of the magnetic field, will enhance the fast ion transport unless measures are taken to mitigate the ripple. The mitigation, in ITER, is handled by ferritic inserts [44, 46]. As the amount of ferritic material inserted inside the walls is selectable, the ripple strength is a variable of the design.

The effect of ripple strength on prompt fusion alpha wall loads was studied using full orbit simulation. As full orbit simulation consumes 50 to 100 times more CPU time than guiding centre simulation, a full slowing down simulation such as [24] is not feasible. The major portion of the ripple induced fast ion losses happens on faster time scales, though, and a 10 ms run was made to study the difference between the full orbit and guiding centre simulations. ITER scenario 4 with a plasma background containing D, T, ^{3}He, He, Be and Ar, with a core temperature of T_e= 24 keV and a core density of n_e= 0.72×10^{20} m^{-3}, was chosen as a reference case as it is rather strongly rippled. The realistic 3D first wall design together with the magnetic field data was used to trace a fusion born α-particle ensemble of about 50 000 particles. Wall loads were calculated from the recorded hits on the 3D wall elements.

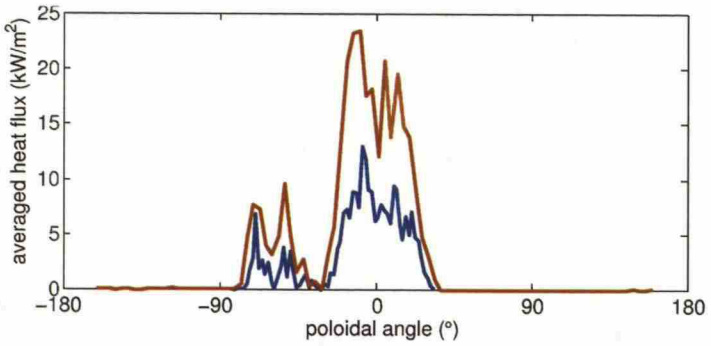

Figure 4.3: Averaged heat load for the unmitigated case with ripple strength of 1.1 %. The full orbit result is shown in red and the guiding centre result in blue. A 100% increase in heat load is observed in full orbit simulation.

In Fig. 4.3, an integrated wall load as a function of the poloidal angle is illustrated for ITER scenario 4 with unmitigated ripple. The maximum ripple strength in this case is δ=1.1%. As can be seen, the guiding centre wall load, shown in blue, is about half of the full orbit wall load, shown in red. The difference between the results is caused by the increased perpendicular transport

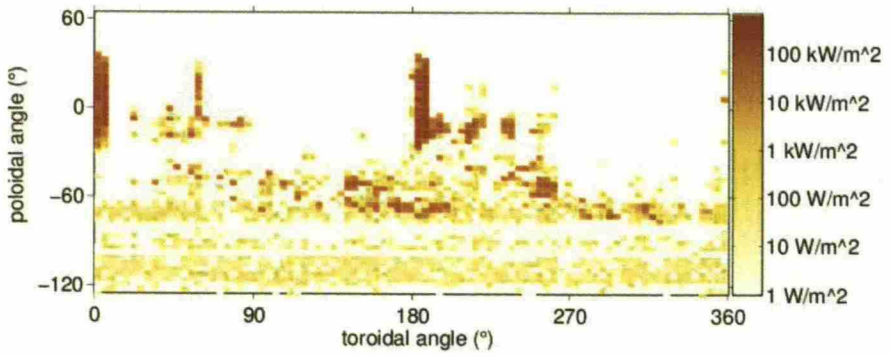

Figure 4.4: Heat load in 2D for the unmitigated case with ripple strength of 1.1 %. Note the hot limiters at ϕ=0°,180°.

due to the toroidal asymmetry of the magnetic field within the Larmor radius of the particle, not taken into account in the guiding centre approximation [7]. Note also that there are spikes at around θ= -60°, where the plasma is close to the wall, and at θ= 0°, where the limiters are located. As the difference between the guiding centre and full orbit simulation is quite notable, guiding centre simulation should not be used for accurate estimates in ITER cases where the ripple is this strong. The 2D full orbit wall load is shown in Fig. 4.4. Two limiters at θ= 0° and ϕ=0°,180° are seen as hot spots. The lower outboard wall region is also clearly visible. In ITER, the design value for the primary wall heat load is typically 0.5 MW/m^2. This number includes all heat sources, e.g. heating by radiation (typically 0.2 MW/m^2).

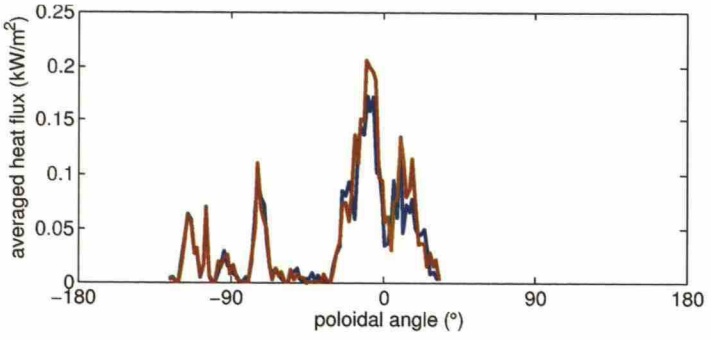

Figure 4.5: Averaged heat load for the optimized inserts case with ripple strength of 0.25%. The full orbit result is shown in red and the guiding centre result in blue. The two match quite nicely, as expected.

Fortunately, the discrepancy between guiding centre and full orbit integration is limited to highly rippled magnetic configurations. This is shown in Fig. 4.5 where the wall loads are show for the same case optimized against magnetic field ripple (δ= 0.25 %). As can be seen, the wall loads are now almost identical and, thus, the guiding centre approximation can be used to simulate the fast ion losses in weakly rippled scenarios in ITER. One should also note that as a result of the optimization, the overall wall load is orders of magnitude smaller than in the strong ripple case shown in Fig. 4.3 [47,48]. The obtained result justifies the use of the guiding centre approximation in slowing-down simulations in ITER scenarios optimized against the magnetic field ripple.

4.3 Accurate hybrid modelling

In the previous section, it was stated that the guiding centre approximation is valid only in weakly rippled fields. If, however, strongly rippled fields or finite Larmor effects in general are being studied, the full orbit integration is observed to be extremely CPU intensive for slowing-down time scales. To alleviate this problem, a hybrid method combining the best features of the guiding centre and full orbit simulation is introduced. It is known that the finite Larmor orbit effects are significant for trapped particles, especially near their turning points where they spend most of their time. In the hybrid method, the orbit-following algorithm switches from guiding centre integration to full orbit integration when approaching the turning point. After the turning point, the full orbit integration (FO) scheme is again swapped to the guiding centre (GC) scheme. The parallel velocity of the particle, $v_{\|}$, scaled to its outboard midplane (maximum) value, v_0, is used to indicate the approaching turning point. Hence, the full orbit integration is turned on when the criteria

$$\frac{v_{\|}}{v_0} \leq v_{\mathrm{limit}}, \tag{4.2}$$

where v_{limit} is a tunable parameter, is satisfied. The parameter v_{limit} should be optimized for the given application. When the parameter is increased, the accuracy and the CPU consumption increase as well. A value v_{limit}=0.3 is used from now on, unless stated otherwise.

The main problem with the hybrid scheme is the transition between the guid-

ing centre and full orbit schemes. It must be extremely accurate in order to avoid numerical drifting. The solution is not obvious, as the two schemes are in fact quite different. The guiding centre particle represents, in principle, an average of an infinite number of real particles, whereas the full orbit particle represents a single real particle. Thus the conservation of adiabatic invariants such as the magnetic moment is rather a feature of the guiding centre than that of the real particle. In fact, the magnetic moment of the particle is not well defined in the full orbit scheme. Even though the location of the particle could be mapped from one picture to the other, it is not enough as the velocity of the particle has to be mapped as well. This is discussed below. The rest of this section describes the status of the hybrid method as it is at the time of this writing. More work is needed to make it accurate enough for hybrid simulations on, e.g., the slowing-down time scale of fusion alpha particles.

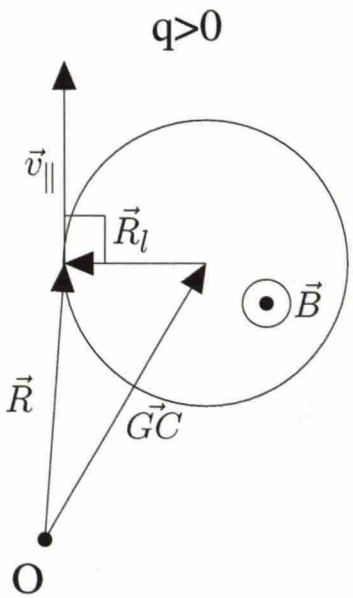

Figure 4.6: Transition from the guiding centre (GC) to the actual location (R) of the particle.

When full orbit integration is begun, at first the location has to be transferred from the guiding centre to the real particle location. As the gyro phase of the particle is unknown in the guiding centre scheme, the real location is not uniquely defined. A random number, α, from the interval $[0, 2\pi]$ is generated

to label the gyro phase angle. After that the particle is moved a distance of one Larmor radius, R_L, in the plane perpendicular to the magnetic field vector $\vec{B}$. The transition is illustrated in Fig. 4.6. Two mutually perpendicular vectors are needed, both in a plane perpendicular to the magnetic field vector. There are several ways to obtain these vectors. One way is to take the cross products of $\vec{B}$ with Cartesian unit vectors $\hat{i}, \hat{j}$ and $\hat{k}$, and then take the longest of the three resulting vectors, $\vec{a}$. This makes sure that the final vector is not a zero vector, which may happen if the magnetic field is parallel to one of the unit vectors. Next, $\vec{a}$ is scaled to unit length, namely

$$\vec{a} = \vec{b} \times \{\hat{i}, \hat{j}, \hat{k}\}, \tag{4.3}$$

where $\vec{b} = \vec{B}/B$ is the magnetic field unit vector. Then the other vector, $\vec{c}$, is produced by taking the cross product of $\vec{a}$ with the magnetic field unit vector

$$\vec{c} = \vec{a} \times \vec{b}. \tag{4.4}$$

The guiding centre location of the particle is given by the vector $\vec{GC}$, which is, of course, known. The real location in Cartesian coordinates, $\vec{R}$, is then given by

$$\vec{R} = \vec{GC} + R_L(\cos(\alpha)\vec{a} + \sin(\alpha)\vec{c}) \tag{4.5}$$

All the vectors in the code are in Cartesian coordinates. After the transition a vector, labelled $\vec{R}_L$, defining the transition by

$$\vec{R}_L = \vec{R} - \vec{GC}, \tag{4.6}$$

is obtained. This vector is scaled to a unit vector $\hat{R}_L$. It is, however, not enough that the position of the particle is known: also the velocity of the particle has to be known in order to trace the orbit of the particle. In the guiding centre scheme, the velocity of the particle is decomposed to two scalars. The parallel velocity, $v_\parallel$, is the component parallel to the magnetic field and the perpendicular velocity, $v_\perp$ is the component perpendicular to it. At this stage, it should be noted that the direction of the perpendicular velocity vector rotates rapidly around the magnetic field line, while the parallel velocity vector changes direction only with the magnetic field vector in a much slower manner. As the positively/negatively charged particle gyrates around the magnetic field vector

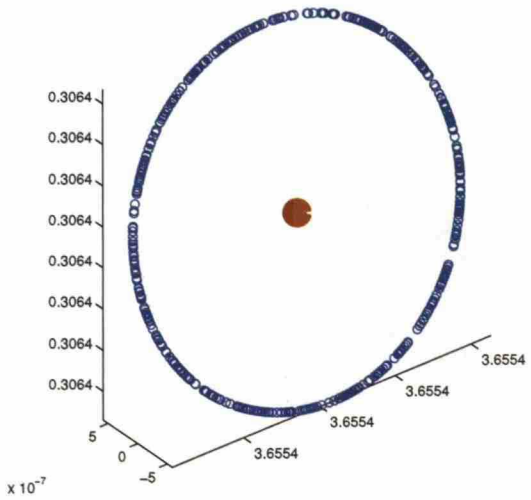

Figure 4.7: Simulated transitions with varying phase angle α: guiding centre in red and initial locations in blue.

clockwise/counterclockwise, the unit perpendicular velocity vector, $\hat{v}_\perp$, defining the direction of the perpendicular velocity is given by

$$\hat{v}_\perp = \pm\left(\hat{R}_L \times \hat{b}\right), \tag{4.7}$$

where the plus/minus sign corresponds to positively and negatively charged particles, respectively. This can be seen from Fig. 4.6 using the right hand rule. Then the final velocity, $\vec{v}$, in the Cartesian coordinates, is given by

$$\vec{v} = v_\parallel \hat{b} + v_\perp \hat{v}_\perp. \tag{4.8}$$

When the switch back to guiding centre integration from full orbit integration is considered, the problem is somewhat different. The three last locations of the particle $\vec{r}(t)$, $\vec{r}(t - \Delta t)$ and $\vec{r}(t - 2\Delta t)$ are available. When the time step is kept small enough, these lie approximately on the same circle in 3D. The task is then to calculate the location of the centre of this circle from the locations and the radius of the circle R_L. At first, it should be noted that as the motion of the particle during these two time steps is assumed to be circular, the acceleration of the particle $\vec{a}$ is in the direction of the circle's unit normal vector $\vec{n}$, namely

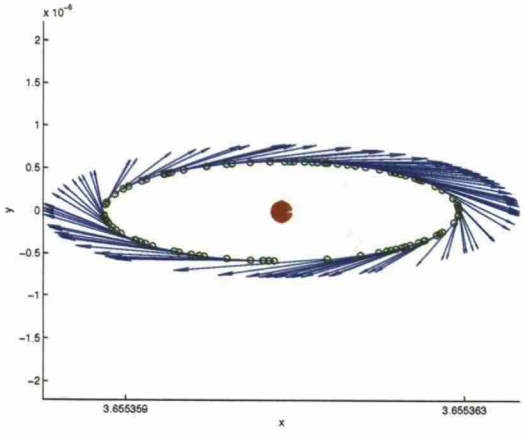

Figure 4.8: Simulated initial perpendicular velocities: guiding centre in red and velocity vectors in blue.

$\vec{n} = \vec{a}/a$. The acceleration of the particle is calculated by the three point finite difference formula for the second derivative of the arbitrary function $f(x)$ given at grid points x_i

$$\frac{\partial^2 f}{\partial x^2} = \frac{f(x+\Delta x) + f(x-\Delta x) - 2f(x)}{\Delta x^2}, \tag{4.9}$$

where Δx is the spacing of the grid. The acceleration $\vec{a}$ is the second derivative of the location $\vec{r}$, and the components $i = 1, 2, 3$ can be calculated separately using Eq. (4.9)

$$a_i(t-\Delta t) = \frac{\partial^2 r_i(t-\Delta t)}{\partial t} = \frac{r_i(t) + r_i(t-2\Delta t) - 2r_i(t-\Delta t)}{\Delta t^2}, \tag{4.10}$$

where Δt is constant time step used in the full orbit integration. It should be noted that the acceleration is evaluated at the point $\vec{r}(t-\Delta t)$. Then it remains to calculate the guiding centre location $\vec{GC}$ from the normalized acceleration vector

$$\vec{GC} = \vec{r}(t-\Delta t) + R_L\vec{n} = \vec{r}(t-\Delta t) + R_L\frac{\vec{a}}{a}, \tag{4.11}$$

where $a = |\vec{a}|$ is the magnitude of the acceleration vector. The situation is illustrated in Fig. 4.9.

As was discussed earlier on, studying finite Larmor radius effects on fast particles in non-axisymmetric backgrounds would be of interest. For this, an

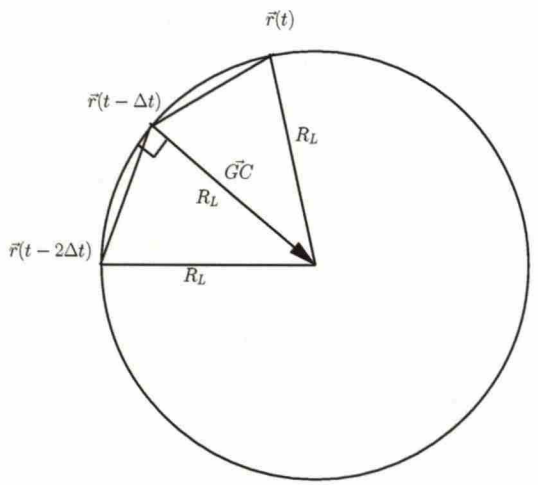

Figure 4.9: Transition from full orbit integration to guiding centre integration.

accurate switch from one method to other is needed near the turning points, where the particle spends most of its time. In Fig. 4.10 the principle of the hybrid scheme is illustrated. Should the fast particles not hit the vessel wall, they are followed until they are thermalized. The time this takes depends heavily on the orbit. On average the slowing down time is around 0.1–1 s. During this process around 5000-10000 poloidal orbits, i.e. 10000-20000 switches, have to be completed. In order to keep the model accurate, it is essential that the switching does not introduce a source of error. In the presently implemented model, which is discussed below, the required accuracy is not reached and the particles tend to drift radially during any simulation which is long compared to the slowing down time.

The switch between the guiding centre solver and the full orbit solver was observed to be good enough for just a couple of transitions. It is, however, possible to enhance the accuracy of the transition. In the reverse switch of the method, from full orbit to guiding centre integration, the treatment of Ref. [49] is followed. There the guiding centre position is given by

$$\vec{GC} = \vec{R} + \vec{R}_1 + \vec{R}_2, \tag{4.12}$$

where in the zeroth order the guiding centre location is given by the gyro loca-

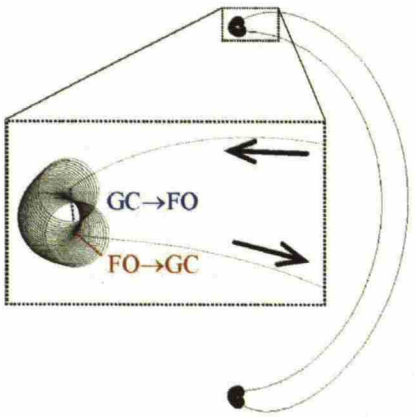

Figure 4.10: Schematic illustration of the hybrid model in action near the turning points.

tion. The first order correction is given by

$$\vec{R}_1 = \frac{\vec{v}(t) \times \hat{b}(t)}{\Omega(t)} \tag{4.13}$$

and the second order correction is given by

$$\begin{aligned} \vec{R}_2 &= \frac{1}{\Omega}\left[\left(v_\parallel \vec{b} + \frac{1}{4}\vec{v}_\perp\right)\left(\vec{v}\times\vec{b}\right)\left(\vec{v}\times\vec{b}\right)\left(v_\parallel \vec{b} + \frac{1}{4}\vec{v}_\perp\right)\right] \dot{\times} \nabla\left(\frac{\vec{b}}{\Omega}\right) \\ &+ \frac{v_\parallel}{\Omega^2}\vec{v}_\perp \cdot \nabla\vec{b} + \frac{\vec{b}}{\Omega^2}\left\{v_\parallel \vec{v}_\perp \cdot \left(\vec{b}\cdot\nabla\vec{b}\right)\right. \\ &+ \left.\frac{1}{8}\left[\vec{v}_\perp\vec{v}_\perp - \left(\vec{v}\times\vec{b}\right)\left(\vec{v}\times\vec{b}\right)\right] : \nabla\vec{b}\right\}, \end{aligned} \tag{4.14}$$

where the following vector conventions have been used: $\vec{x}\vec{y} : \overleftrightarrow{M} = \vec{y}\cdot\overleftrightarrow{M}\cdot\vec{x}$ and $\vec{x}\vec{y}\dot{\times}\overleftrightarrow{M} = \vec{x}\times\left(\vec{y}\cdot\overleftrightarrow{M}\right)$.

As the guiding centre location is unknown, the magnetic field related quantities in Eqs. (4.13) and (4.14) are evaluated at the full orbit location. The method based on Eq. (4.12) is called the vxb-method. Furthermore, the accuracy of the transition from guiding centre to real particle location can be enhanced by inverting Eq. (4.12) to give $\vec{R}$, i.e.

$$\vec{R} = \vec{GC} - \vec{R}_1 - \vec{R}_2. \tag{4.15}$$

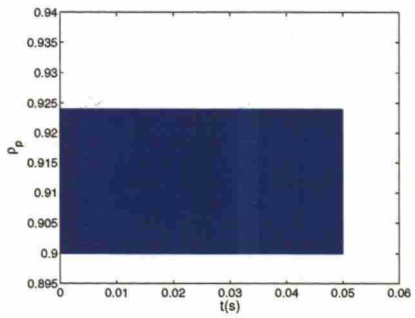

Figure 4.11: Pure guiding centre simulation stays precisely at the same flux surface. The orbit is a typical fusion born alpha launched from the outer midplane with pitch ξ=0.3 and radial coordinate ρ_p=0.9.

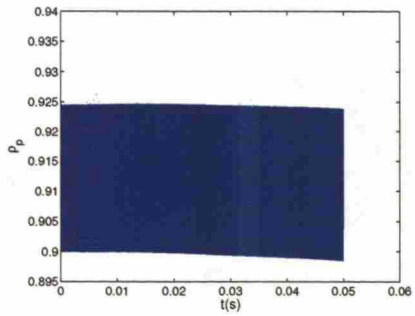

Figure 4.12: Full orbit simulation is accurate enough to be used in production runs with collisions. The orbit is a typical fusion born alpha launched from the outer midplane with pitch ξ=0.3 and radial coordinate ρ_p=0.9.

In this case the magnetic field related quantities are evaluated at the guiding centre location and, therefore, the whole transition process is asymmetric.

The calculation of the velocity components is inherently difficult. The reason for this is that there is no clear mapping between the guiding centre and the full orbit pictures. The former is, by definition, an average of an infinite number of the latter. In the guiding centre approach, both the magnetic moment and the total energy are conserved. The magnetic moment is, by definition, a quantity of the guiding centre, not the instantaneous full orbit location. The total energy, however, should be conserved in the guiding centre to full orbit shift as well. Doing this only fixes the magnitude of the total velocity, leaving the freedom to choose the velocity components. It was attempted to keep the particle's magnetic moment constant, thus fixing $v_\perp$, with rather poor results. The orbits were

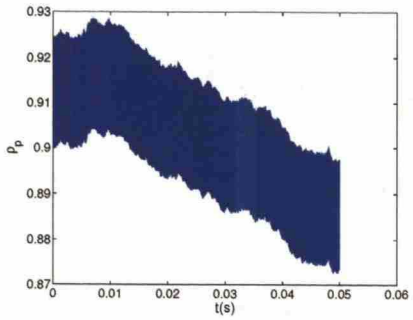

Figure 4.13: The hybrid scheme is tested with a reverse shift method based on Eq. (4.12). The orbit is a typical fusion born alpha launched from the outer midplane with pitch ξ=0.3 and radial coordinate ρ_p=0.9.

not stable enough for long simulation times. Furthermore, when the shift from full orbit to the guiding centre was carried out too close to the banana reflection point, keeping the magnetic moment fixed could lead to a situation where the perpendicular velocity exceeded the total velocity. For these reasons the magnetic moment appears not to be the appropriate physical quantity for fixing the relative magnitude of the velocity components. So far, a satisfactory solution to the above mentioned problems has not been found. In the simulation presented throughout this work, the conservation of magnetic moment is used to obtain a new perpendicular velocity and the conservation of energy is used to obtain a new parallel velocity. The research is, however, ongoing.

To make the problems with the longer time scales more transparent, a 50 ms simulation with three different schemes is presented: i) using pure guiding centre integration, ii) using pure full orbit integration, iii) using hybrid integration with switches handled by the vxb-method. The background is the axisymmetric ITER discharge #585. As can be seen from Fig. 4.11, the guiding centre stays at the same flux surface extremely accurately while the pure full orbit slowly drift radially near the end of the simulation, as shown in Fig. 4.12. The hybrid scheme, as shown in Fig. 4.13, suffers from intolerable numerical diffusion. The CPU requirements on the different schemes for the same simulation are presented in Table 4.1. As can be seen, even the hybrid schemes are quite CPU-consuming compared to the CPU-efficient guiding centre integration. The full orbit integration scheme is computationally about 180 times slower than the guiding centre scheme. The production runs usually contain around 100 000

Table 4.1: CPU time consumption for different orbit following schemes.

Scheme	pure GC	pure FO	FO-GC hybrid
CPU time (s)	17.2	3068	748

particles and thus using full orbit integration would consume excessive amounts of CPU time.

4.4 Accurate wall load distributions

In this section we will discuss a scheme where full orbit integration is used to recalculate the last time step after the guiding centre comes within a Larmor radius of the wall structure. In earlier work, the wall collision check in ASCOT was done so that the two last guiding centre locations were shifted one Larmor radius towards the nearest wall element(s). If the line between these two shifted guiding centre locations intersected any vacuum vessel wall elements, wall collision had occurred. This kind of wall hit check may produce inaccurate wall hit positions since the guiding centre step may be relatively long. The transition from guiding centre simulation to full orbit simulation needs to be done just once. Hence, a small numerical error made in the transition does not cumulate. The change of the simulation method is handled so that when the guiding centre orbit approaches within a Larmor radius of a wall element, the particle is returned one time step backwards in time and full orbit simulation is switched on. The full orbit wall collision check is very accurate, since the full orbit steps are small compared to guiding centre steps. Moreover, the simplistic Larmor radius shift is no more needed.

To clarify this, an extreme case is shown where the wall hit locations obtained by the full orbit collision check and guiding centre check are clearly different. A 3.5 MeV alpha particle was launched from the outer midplane with ρ_p=0.95 and ξ=-0.3. The background is the non-axisymmetric ITER Scenario 4 [9]. The guiding centre trace and the 3D vacuum vessel elements (divertor plates in red) are shown in Fig. 4.14(a). A close-up of the wall hit locations, is shown in Fig. 4.14(b). The dotted and solid lines correspond to the guiding centre trace with the old wall collision check and the GC solver trace combined with the new full orbit wall collision check, respectively. We have labeled the wall hit location obtained using the old method with a red cross. Note that the

(a) (b)

Figure 4.14: (a) A prompt ripple loss 3.5 MeV alpha particle orbit. The particle is launched from the outer midplane with pitch ξ=-0.3 and radial coordinate ρ_p=0.95. (b) A detail shows the switch from guiding centre integration method to full orbit integration. The guiding centre trace (red dotted line) is shown together with the final wall hit position (red dot). The full orbit wall hit position is at the end of the solid line. The view is from the middle of the plasma.

collision in Fig. 4.14(b) is viewed from the centre of the plasma. As can be seen, in this case the wall hit locations are in different vacuum vessel elements. This, of course, has an effect when wall loads are calculated.

Chapter 5

Numerical model for magnetic islands

In order to validate the simulations accurately to the experiments in current devices, it is important to include all relevant fast ion physics in the simulation model. ASCOT models neoclassical physics accurately, but omits the interaction of the fast ions with MHD instabilities. As these instabilities not only occur in almost every experiment but also largely affect the fast ion transport properties, they should be included in the treatment of fast ions in ASCOT as well. This Chapter presents the implementation of such a model. It concentrates on neoclassical tearing modes, which are by far the easiest MHD instability to implement in a simulation.

A detailed derivation of relativistic equations of motion for a generalized perturbation is presented, and the equations are simplified assuming a magnetic vector potential perturbation parallel to the magnetic field line.

5.1 Introduction to plasma instabilities

The idea of MHD, see e.g. Refs. [50, 51], is to describe the plasma as a single fluid where the forces acting on the fluid elements are caused by the magnetic field and currents in the plasma. The stability of the tokamak has two basic aspects. Firstly, there is an internal balance between the forces due to the magnetic field and the pressure gradient of the plasma, namely

$$\vec{j} \times \vec{B} = \nabla p, \tag{5.1}$$

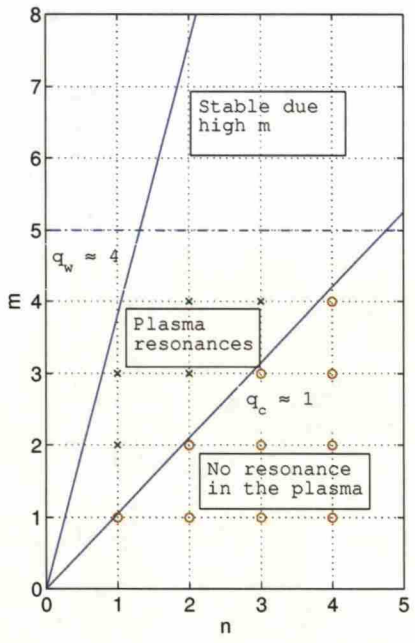

Figure 5.1: Allowed modes in a plasma with q values limited from core value (q_c) to the q value at the edge (q_w).

where $\vec{j}$ is the current density and p is the plasma pressure. Secondly, there is the shape and position of the plasma determined by the external coil currents which, among other things, allow the X-point geometry of the divertor configuration. The basic reason for instabilities in tokamaks are the gradients in current density and pressure. The resulting instabilities are usually divided into ideal modes, in which the plasma can be assumed perfectly conducting, and resistive modes, which occur only in resistive plasmas. The modes are labeled by their mode numbers. In case of the periodic perturbation, the modes can be described by the toroidal harmonics

$$\xi \propto \exp^{i(m\theta - n\phi - \omega t)}, \tag{5.2}$$

where m is the poloidal mode number, n the toroidal mode number and ω the frequency of the mode. Since the instabilities are stabilized by the effect of magnetic field line bending, increasing with m, instabilities occur on the magnetic surface, where the magnetic field helix matches that of the mode. These

surfaces are referred to as resonance surfaces satisfying $q = m/n$, where q is the safety factor. The number of allowed modes is limited by the range of q values in the plasma and the fact that when m increases the magnetic field line bending stabilizes the mode. This is illustrated schematically in Fig. 5.1, where just 5 modes can occur in the plasma.

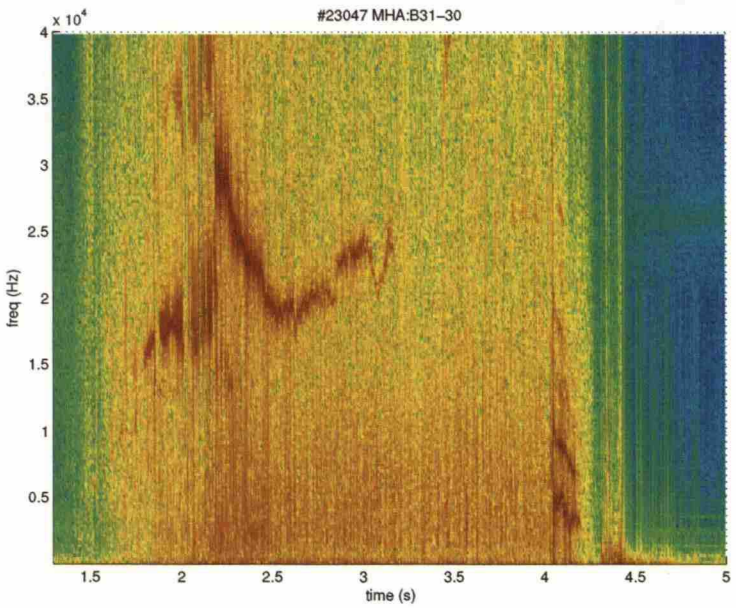

Figure 5.2: Spectrogram from a magnetic pick-up coil in ASDEX Upgrade shot # 23047. The instability with $\omega \approx 20$ kHz is most likely a NTM.

The modes can be distinguished according to their frequencies as well. As can be understood from Eq. (5.2), the mode rotates with the frequency ω. Hence, the frequency of the mode can be observed from the Mirnov coil data [52]. In Fig. 5.2, a MHD mode with frequency around 20 - 25 kHz is shown for ASDEX Upgrade shot # 23047. In this thesis, low frequency neoclassical tearing modes (NTM's) with $\omega \approx$ 5-25 kHz and Alfven eigenmodes (AE) with $\omega \approx$ 50-250 kHz are discussed and a numerical model for implementation in ASCOT is presented for NTM's.

5.2 The relativistic Hamiltonian formalism

In this Section, a particle with relativistic energy is considered in the Hamiltonian formalism. In the next Section, the formalism is used to derive the equations of motion for the particle. While the ions can usually be treated classically, relativistic treatment is needed, e.g., to model fast electrons properly. Lagrangian mechanics, which also guarantees the conservation of momentum and energy, is taken as a starting point.

The approach is to use generalized coordinates $q(t)$ and their total derivatives $\dot{q}(t)$. Together these are called phase space coordinates. The idea in Lagrangian mechanics is to use variational calculus on the action of the Lagrangian and derive a normal differential equation for the phase space coordinates by minimizing the action integral. The action is defined by

$$S(q) = \int_a^b L(t, q(t), \dot{q}(t))dt, \tag{5.3}$$

where the L is called a Lagrangian. By varying q in the action integral in such a way that the variation vanishes at the end points the following identities are obtained

$$\begin{aligned} \delta S &= \int \left(\frac{\partial L}{\partial q}\delta q + \frac{\partial L}{\partial \dot{q}}\delta\dot{q} \right) dt \\ &= \int \left(\frac{\partial L}{\partial q}\delta q + \frac{\partial L}{\partial \dot{q}}\frac{d\delta q}{dt} \right) dt \\ &= \Big/_a^b \frac{\partial L}{\partial \dot{q}}\delta q + \int_a^b (\frac{\partial L}{\partial q} - \frac{d}{dt}\frac{\partial L}{\partial \dot{q}})\delta q \\ &= \int_a^b \left(\frac{\partial L}{\partial q} - \frac{d}{dt}\frac{\partial L}{\partial \dot{q}} \right) \delta q. \end{aligned} \tag{5.4}$$

As the variation of action (5.4) for arbitrary δq is required to vanish, the integrand has to vanish as well. Thus, the Euler-Lagrange equation for phase space coordinates

$$\frac{\partial L}{\partial Z^\alpha} - \frac{d}{dt}\frac{\partial L}{\partial \dot{Z}^\alpha}, \tag{5.5}$$

is obtained, where the phase space coordinates are denoted with Z^α to distin-

guish each component. It is also important to remember that each coordinate is an independent function of time only, as can be seen from Equation (5.3).

The Hamiltonian formalism is obtained by writing the Lagrangian as a function of so-called canonical coordinates. The Lagrangian then reads

$$L = \sum_i P_i \dot{q}_i - H, \tag{5.6}$$

where P_i and q_i are the canonical coordinates for momentum and location, respectively. The relativistic particle Hamiltonian being [31]

$$\begin{aligned} H &= \gamma mc^2 + q\Phi \\ &= mc^2 \sqrt{1 + \frac{2\mu B}{mc^2} + \left(\frac{p_\parallel}{mc}\right)^2} + q\Phi, \end{aligned} \tag{5.7}$$

where Φ is the electric scalar potential and $p_\parallel$ is the parallel momentum, the suitable Lagrangian function reads [31]

$$L = \left(\frac{q}{c}\boldsymbol{A} + p_\parallel \boldsymbol{b}\right) \cdot \dot{\boldsymbol{R}} + \frac{mc\mu}{q}\dot{\xi} - H, \tag{5.8}$$

where ξ is the gyro-phase. Inserting the Hamiltonian from Eq.(5.7) to Eq.(5.8), it is immediately seen that the canonical momentum becomes

$$\boldsymbol{P} = p_\parallel \boldsymbol{B}/B + q\boldsymbol{A}. \tag{5.9}$$

The equations of motion can now be derived using this Lagrangian and the Euler-Lagrange equation (5.5). The result is the following set of equations:

$$\begin{aligned} \dot{P}_\theta &= -\partial H/\partial\theta, \quad \dot{\theta} = \partial H/\partial P_\theta \\ \dot{P}_\zeta &= -\partial H/\partial\zeta, \quad \dot{\zeta} = \partial H/\partial P_\zeta. \end{aligned} \tag{5.10}$$

In order to derive explicit forms for these, the partial derivatives appearing on the right hand sides of Eq. (5.14) must be calculated.

5.3 Equations of motion in magnetic coordinates

In this Section, the equations of motion in Hamiltonian formalism are considered. Boozer originally showed that with a particular choice of coordinates the magnetic field line becomes straight [28, 53] and this idea is utilized here as well. Now H is a function of $p_\parallel$, B and Φ. To include the magnetic coordinates (χ, θ, ζ), the covariant presentation for the vector potential and the magnetic field is used. This means that the magnetic field is given by $\boldsymbol{B} = G\nabla\zeta + I\nabla\theta + \beta\nabla\chi$. In the contravariant form the magnetic field is $\boldsymbol{B} = \nabla\times(\psi\nabla\theta - \chi\nabla\zeta) = \nabla\times\boldsymbol{A}$, where ψ is the toroidal magnetic flux. Thus the canonical magnetic vector potential can be written as

$$\boldsymbol{A} = \psi\nabla\theta - \chi\nabla\zeta + \tilde{\boldsymbol{A}}, \tag{5.11}$$

where the most general perturbative term $\tilde{\boldsymbol{A}} = \tilde{A}_\chi\nabla\chi + \tilde{A}_\theta\nabla\theta + \tilde{A}_\zeta\nabla\zeta$ is included. The so-called parallel gyro radius is defined by

$$\rho_\parallel = \frac{p_\parallel}{qB}. \tag{5.12}$$

Now the canonical momenta can be obtained by writing the Lagrangian in a way similar to finding Eq. (5.9). Component-wise, the momenta are given by

$$\begin{aligned} P_\theta &= q\{I\rho_\parallel + \psi + \tilde{A}_\theta\} \\ P_\zeta &= q\{G\rho_\parallel - \chi + \tilde{A}_\zeta\}. \end{aligned} \tag{5.13}$$

The canonical momenta are no longer functions of canonical position θ and ζ as the flux functions I and G are functions of χ only. Thus we now have proper momenta and position. The reason why the third component of the canonical momenta, P_χ, is left out, is discussed in detail in Ref. [54] in chapter 3.2. The main idea is that a new transformation of the guiding center is done in second order and this transforms the Lagrangian into a form where only P_θ and P_ζ arise while leaving the Hamiltonian as it is.

The equations of motion can now be derived from the familiar equations

arising from the Hamiltonian formalism

$$\begin{aligned} \dot{P}_\theta &= -\partial H/\partial\theta, \quad \dot{\theta} = \partial H/\partial P_\theta \\ \dot{P}_\zeta &= -\partial H/\partial\zeta, \quad \dot{\zeta} = \partial H/\partial P_\zeta. \end{aligned} \tag{5.14}$$

For the derivation of the actual equations of motion it has to be noted that the Hamiltonian is now a function of different variables which further are functions of the magnetic coordinates and the perturbation. This has to be taken into account when performing the differentiation by chain rule. The equations of motion can be written explicitly as

$$\dot{P}_\theta = -\frac{\partial H}{\partial B}\frac{\partial B}{\partial \theta} - \frac{\partial H}{\partial \Phi}\frac{\partial \Phi}{\partial \theta} - \frac{\partial H}{\partial \rho_\parallel}\left(\frac{\partial \rho_\parallel}{\partial \tilde{A}_\theta}\frac{\partial \tilde{A}_\theta}{\partial \theta} + \frac{\partial \rho_\parallel}{\partial \tilde{A}_\zeta}\frac{\partial \tilde{A}_\zeta}{\partial \theta}\right) \tag{5.15}$$

$$\dot{P}_\zeta = -\frac{\partial H}{\partial B}\frac{\partial B}{\partial \zeta} - \frac{\partial H}{\partial \Phi}\frac{\partial \Phi}{\partial \zeta} - \frac{\partial H}{\partial \rho_\parallel}\left(\frac{\partial \rho_\parallel}{\partial \tilde{A}_\theta}\frac{\partial \tilde{A}_\theta}{\partial \zeta} + \frac{\partial \rho_\parallel}{\partial \tilde{A}_\zeta}\frac{\partial \tilde{A}_\zeta}{\partial \zeta}\right) \tag{5.16}$$

$$\dot{\theta} = \frac{\partial H}{\partial B}\frac{\partial B}{\partial \chi}\frac{\partial \chi}{\partial P_\theta} + \frac{\partial H}{\partial \rho_\parallel}\frac{\partial \rho_\parallel}{\partial P_\theta} + \frac{\partial H}{\partial \Phi}\frac{\partial \Phi}{\partial \chi}\frac{\partial \chi}{\partial P_\theta} \tag{5.17}$$

$$\dot{\zeta} = \frac{\partial H}{\partial B}\frac{\partial B}{\partial \chi}\frac{\partial \chi}{\partial P_\zeta} + \frac{\partial H}{\partial \rho_\parallel}\frac{\partial \rho_\parallel}{\partial P_\zeta} + \frac{\partial H}{\partial \Phi}\frac{\partial \Phi}{\partial \chi}\frac{\partial \chi}{\partial P_\zeta}. \tag{5.18}$$

The fields are functions of θ and ζ, and thus derivatives such as $\partial\theta/\partial P_\theta$ vanish because the other term is a canonical variable and the other one is a canonical momentum.

There are a couple of nontrivial terms to calculate in Eqs. (5.17) and (5.18), but with partial differentiation these can be solved. From Eqs. (5.13), $\rho_\parallel$ can be eliminated to obtain

$$GP_\theta - IP_\zeta = q(G\psi + I\chi + G\tilde{A}_\theta - I\tilde{A}_\zeta) \tag{5.19}$$

Differentiating this equation implicitly with respect to P_θ, the following identity

is obtained:

$$\frac{\partial \chi}{\partial P_\zeta} = -\frac{I}{D}, \tag{5.20}$$

where

$$D = q\{I + q_s G + \rho_\parallel (I'G - G'I) + G\tilde{A}_\theta - I\tilde{A}_\zeta\}, \tag{5.21}$$

q_s is the safety factor defined as $q_s(\chi) = d\psi/d\chi$ and a prime denotes derivative with respect to χ. Exactly in the same way, by taking the partial derivative with respect to P_θ, the identity

$$\frac{\partial \chi}{\partial P_\theta} = \frac{G}{D} \tag{5.22}$$

is obtained. To get the derivatives of $\rho_\parallel$, the same method as above is used. Taking the partial derivatives of (5.13) and applying (5.20) and (5.22), the following identities emerge:

$$\frac{\partial \rho_\parallel}{\partial P_\zeta} = \frac{q_s + \rho_\parallel I' + \tilde{A}'_\theta}{D} \tag{5.23}$$

$$\frac{\partial \rho_\parallel}{\partial P_\theta} = \frac{1 - \rho_\parallel G' - \tilde{A}'_\zeta}{D}. \tag{5.24}$$

Before substituting the derivatives back to the equations of motion (5.15-5.18), one useful observation is made. Since in Eq. (5.19) I and G are functions only of χ and $d\psi = q_s(\chi)d\chi$, it is clear that Eq. (5.19) implicitly defines $\chi \equiv \chi(P_\theta, P_\zeta, \tilde{A}_\theta, \tilde{A}_\zeta)$. Thus we get the equation of motion for χ as

$$\begin{aligned}\dot{\chi} = &\frac{\partial \chi}{\partial P_\theta}\dot{P}_\theta + \frac{\partial \chi}{\partial P_\zeta}\dot{P}_\zeta + \frac{\partial \chi}{\partial \tilde{A}_\theta}\frac{\partial \tilde{A}_\theta}{\partial \theta}\dot{\theta} + \frac{\partial \chi}{\partial \tilde{A}_\zeta}\frac{\partial \tilde{A}_\zeta}{\partial \zeta}\dot{\zeta} + \\ &\frac{\partial \chi}{\partial \tilde{A}_\theta}\frac{\partial \tilde{A}_\theta}{\partial \zeta}\dot{\zeta} + \frac{\partial \chi}{\partial \tilde{A}_\zeta}\frac{\partial \tilde{A}_\zeta}{\partial \theta}\dot{\theta}.\end{aligned} \tag{5.25}$$

Therefore, a couple of more partial derivatives are needed. The missing two appearing in the Eq. (5.25) are found by similar means as the previous ones,

taking partial derivatives of Eq. (5.19). The result reads

$$\begin{aligned} \frac{\partial \chi}{\partial \tilde{A}_\zeta} &= \frac{I}{D} \\ \frac{\partial \chi}{\partial \tilde{A}_\theta} &= \frac{-G}{D}. \end{aligned} \tag{5.26}$$

Using these, the partial derivatives missing from the equations of motion (5.15-5.18) are obtained, i.e.

$$\frac{\partial \rho_\parallel}{\partial \tilde{A}_\theta} = \frac{-1 + G'\rho_\parallel + \tilde{A}'_\zeta}{D} \tag{5.27}$$

$$\frac{\partial \rho_\parallel}{\partial \tilde{A}_\zeta} = \frac{-q_s - I'\rho_\parallel - \tilde{A}'_\theta}{D} \tag{5.28}$$

The equation of motion for $\rho_\parallel$ is obtained by taking the time derivative of Eq. (5.14) and using the previous results for the partial derivatives.

At this point, a relation to the classical case can be made. So far the only connection to relativity has been the form of the Hamiltonian. Hence, in the classical case the generalized momenta and position $(P_\theta, \theta, P_\zeta, \zeta)$ are exactly the same as in the relativistic case, as can be seen from Ref. [55]. Thus all the derivatives derived so far apply also for the classical case and remain unchanged. The rest of the partial derivatives are simple to calculate directly from the Hamiltonian (5.7):

$$\begin{aligned} \frac{\partial H}{\partial B} &= \frac{\mu}{\gamma} + \frac{q^2 B \rho_\parallel^2}{\gamma m} \\ \frac{\partial H}{\partial \rho_\parallel} &= \frac{q^2 B^2 \rho_\parallel}{\gamma m} \\ \frac{\partial H}{\partial \alpha} &= -\frac{q^2 B^2 \rho_\parallel}{\gamma m} \\ \frac{\partial H}{\partial \Phi} &= q, \end{aligned} \tag{5.29}$$

where q is the charge of the particle.

Because the classical Hamiltonian can be written simply as

$$\begin{aligned} H &= \frac{p_\parallel^2}{2m} + \mu B + q\Phi \\ &= \frac{e^2 B^2 \rho_\parallel^2}{2m} + \mu B + q\Phi, \end{aligned} \tag{5.30}$$

it is easy to see that the relativistic equations reduce to the classical ones by setting γ=1. By inserting the above relations for the partial derivatives to the equations of motion (5.15-5.18), the final form of the relativistic equations of motion is obtained:

$$\begin{aligned} \dot{P}_\theta = &-\left(\frac{\mu}{\gamma} + \frac{q^2 B \rho_\parallel^2}{\gamma m}\right)\frac{\partial B}{\partial \theta} - q\frac{\partial \Phi}{\partial \theta} \\ &- \frac{q^2 B^2 \rho_\parallel}{\gamma m D}\left(\left(-1 + G'\rho_\parallel + \tilde{A}'_\zeta\right)\frac{\partial \tilde{A}_\theta}{\partial \theta} - \left(q_s + I'\rho_\parallel + \tilde{A}'_\theta\right)\frac{\partial \tilde{A}_\zeta}{\partial \theta}\right) \end{aligned} \tag{5.31}$$

$$\begin{aligned} \dot{P}_\zeta = &-\left(\frac{\mu}{\gamma} + \frac{q^2 B \rho_\parallel^2}{\gamma m}\right)\frac{\partial B}{\partial \zeta} - q\frac{\partial \Phi}{\partial \zeta} \\ &- \frac{q^2 B^2 \rho_\parallel}{\gamma m}\left(\left(-1 + G'\rho_\parallel + \tilde{A}'_\zeta\right)\frac{\partial \tilde{A}_\theta}{\partial \zeta} - \left(q_s + I'\rho_\parallel + \tilde{A}'_\theta\right)\frac{\partial \tilde{A}_\zeta}{\partial \zeta}\right) \end{aligned} \tag{5.32}$$

$$\dot{\theta} = \frac{1}{D}\left(\left(\frac{\mu}{\gamma} + \frac{q^2 B \rho_\parallel^2}{\gamma m}\right)GB' + \frac{q^2 B^2 \rho_\parallel}{\gamma m}\left(1 - G'\rho_\parallel - \tilde{A}'_\zeta\right) + qG\Phi'\right) \tag{5.33}$$

$$\dot{\zeta} = \frac{1}{D}\left(-\left(\frac{\mu}{\gamma} + \frac{q^2 B \rho_\parallel^2}{\gamma m}\right)IB' + \frac{q^2 B^2 \rho_\parallel}{\gamma m}\left(q_s + I'\rho_\parallel + \tilde{A}_\theta\right) - qI\Phi'\right) \tag{5.34}$$

$$\dot{\chi} = \frac{1}{D}\left(G\dot{P}_\theta - I\dot{P}_\zeta + \left(I\frac{\partial \tilde{A}_\zeta}{\partial \theta} - G\frac{\partial \tilde{A}_\theta}{\partial \theta}\right)\dot{\theta} + \left(I\frac{\partial \tilde{A}_\zeta}{\partial \zeta} - G\frac{\partial \tilde{A}_\theta}{\partial \zeta}\right)\dot{\zeta}\right) \tag{5.35}$$

$$\dot{\rho}_\parallel = \frac{1}{I}\left(\frac{\dot{P}_\theta}{q} - \frac{\partial \tilde{A}_\theta}{\partial \theta}\dot{\theta} - \frac{\partial \tilde{A}_\theta}{\partial \zeta}\dot{\zeta} - \frac{\partial \tilde{A}_\theta}{\partial t} - \left(1 + \tilde{A}'_\theta + I'\rho_\parallel\right)\dot{\chi}\right). \tag{5.36}$$

This set of equations can be simplified if the perturbation is assumed small. Then the derivatives of the perturbation are small as well, and the product of two such terms is neglected in the first order. Hence, the set of equations above

is correct to the second order.

5.4 Perturbation parallel to $\boldsymbol{B}$

Eqs. (5.31-5.36) can be further simplified by making an assumption that the perturbation is parallel to the magnetic field, i.e. $\tilde{\boldsymbol{A}} = \alpha(\chi,\theta,\zeta,t)\boldsymbol{B}$. This corresponds to the perturbation in the radial , i.e. $\nabla\psi$, direction, as in e.g. low-β Alfven waves or neoclassical tearing modes (NTM). In this case, the equations of motion can be derived [31,56] in much the same manner as above. They read

$$\dot{P}_\theta = -\left(\frac{\mu}{\gamma} + \frac{q^2 B\rho_\parallel^2}{\gamma m}\right)\frac{\partial B}{\partial\theta} - q\frac{\partial\Phi}{\partial\theta} + \frac{q^2B^2\rho_\parallel}{\gamma m}\frac{\partial\alpha}{\partial\theta} \tag{5.37}$$

$$\dot{P}_\zeta = -\left(\frac{\mu}{\gamma} + \frac{q^2 B\rho_\parallel^2}{\gamma m}\right)\frac{\partial B}{\partial\zeta} - q\frac{\partial\Phi}{\partial\zeta} + \frac{q^2B^2\rho_\parallel}{\gamma m}\frac{\partial\alpha}{\partial\zeta} \tag{5.38}$$

$$\dot{\theta} = \left(\frac{\mu}{\gamma} + \frac{q^2 B\rho_\parallel^2}{\gamma m}\right)\frac{G}{D}\frac{\partial B}{\partial\chi} + \frac{q^2B^2\rho_\parallel}{\gamma mD}\left(1 - G'(\rho_\parallel+\alpha) - G\frac{\partial\alpha}{\partial\chi}\right) + q\frac{G}{D}\frac{\partial\Phi}{\partial\chi} \tag{5.39}$$

$$\dot{\zeta} = -\left(\frac{\mu}{\gamma} + \frac{q^2 B\rho_\parallel^2}{\gamma m}\right)\frac{I}{D}\frac{\partial B}{\partial\chi} + \frac{q^2B^2\rho_\parallel}{\gamma mD}\left(q_s + I'(\rho_\parallel+\alpha) + I\frac{\partial\alpha}{\partial\chi}\right) - q\frac{I}{D}\frac{\partial\Phi}{\partial\chi} \tag{5.40}$$

$$\dot{\chi} = \frac{G}{D}\dot{P}_\theta - \frac{I}{D}\dot{P}_\zeta \tag{5.41}$$

$$\dot{\rho}_\parallel = \frac{1-(\rho_\parallel+\alpha)G'}{D}\dot{P}_\theta + \frac{q_s + I'(\rho_\parallel+\alpha)}{D}\dot{P}_\zeta - \frac{\partial\alpha}{\partial\chi}\dot{\chi} - \frac{\partial\alpha}{\partial\theta}\dot{\theta} - \frac{\partial\alpha}{\partial\zeta}\dot{\zeta} - \frac{\partial\alpha}{\partial t}. \tag{5.42}$$

This is the set of equations implemented in ASCOT. The parameter $\alpha = \alpha(\chi,\theta,\zeta,t)$ is the only thing that has to be given. It should be, however, noted that α is typically oscillating function of the angle coordinates whereas the radial dependency is not currently understood in detail. Hence, the radial dependency is typically obtained by parametrized formulas by fitting the parameters to corresponding experimental results, e.g. island width and location.

5.5 Neoclassical tearing modes

In the case of the NTM, the perturbation has a simple form

$$\alpha(\chi,\theta,\zeta,t)=\sum_{n,m}A_{m,n}(\chi)\cos(m\theta-n\zeta), \tag{5.43}$$

where the amplitudes $A_{m,n}$ for different perturbations can be functions of the radial coordinate. It should be noted that the perturbation is assumed to be static, which is a good approximation since the rotation of the mode is slow compared to the fast movement of the test particles. The integers n and m are the toroidal and poloidal harmonics of the perturbation, respectively. To describe the perturbation, only the radial functions together with the mode numbers are needed. The partial derivatives of this perturbation needed in the equations of motion Eqs. (5.37-5.42) can be analytically calculated, resulting in the following set of equations

$$\frac{\partial\alpha}{\partial\chi}=\frac{\partial A_{m,n}}{\partial\chi}\cos(m\theta-n\zeta) \tag{5.44}$$

$$\frac{\partial\alpha}{\partial\theta}=-mA_{m,n}(\chi)\sin(m\theta-n\zeta) \tag{5.45}$$

$$\frac{\partial\alpha}{\partial\zeta}=nA_{m,n}(\chi)\sin(m\theta-n\zeta) \tag{5.46}$$

$$\frac{\partial\alpha}{\partial t}=0, \tag{5.47}$$

where only one term from the sum in Eq. (5.43) is considered. To make the model complete, two different expressions for the radial profiles $A_{m,n}(\chi)$ are presented. The first one [54] describes so-called resistive modes and is a theory based parametrization, namely

$$\begin{aligned}A_{m,n}(\chi)=&\rho_{m,n}\alpha\left(\frac{\chi}{\chi_{m,n}}\right)^{m/2}\left(1-\beta\left(\frac{\chi}{\chi_{m,n}}\right)^{1/2}\right) \quad ,\text{for}\,\chi\le\chi_{m,n}\\ A_{m,n}(\chi)=&\rho_{m,n}\frac{\alpha(1-\beta)-\gamma+\gamma\left(\frac{\chi}{\chi_{m,n}}\right)^{1/2}}{(\chi/\chi_{m,n})^{(m+1)/2}} \quad ,\text{for}\,\chi>\chi_{m,n}\end{aligned} \tag{5.48}$$

The parameters $\rho_{m,n}$, α, β and γ are fixed so that the island width, the island position and the radial perturbation field strength correspond to the ones ob-

tained from experimental data. The position and width are obtained by electron cyclotron emission (ECE) measurements, while the perturbation field strength is obtained by motional Stark effect (MSE) measurement. The radial partial derivative of this perturbation is given by

$$\begin{aligned}\frac{\partial A_{m,n}(\chi)}{\partial \chi} =& \frac{\rho_{m,n}\alpha m \chi^{m/2-1}}{2(\chi_{m,n})^{m/2}}\left(1-\beta\left(\frac{\chi}{\chi_{m,n}}\right)^{1/2}\right) \\ & -\frac{\beta\rho_{m,n}\alpha}{2(\chi_{m,n})^{1/2}}\chi^{-1/2}\left(\frac{\chi}{\chi_{m,n}}\right)^{m/2}, \text{ for } \chi \le \chi_{m,n} \qquad (5.49)\\ \frac{\partial A_{m,n}(\chi)}{\partial \chi} =& \frac{\rho_{m,n}\gamma\chi^{-1/2}}{2(\chi_{m,n})^{1/2}}\left(\frac{\chi}{\chi_{m,n}}\right)^{-(m+1)/2} - \frac{2\rho_{m,n}\chi^{-(m+1)/2-1}}{(m+1)(\chi_{m,n})^{-(m+1)/2}}\times \\ & \times\left(\alpha(1-\beta)-\gamma+\gamma\left(\frac{\chi}{\chi_{m,n}}\right)^{1/2}\right), \text{ for } \chi > \chi_{m,n}. \qquad (5.50)\end{aligned}$$

The second radial perturbation profile describes the ideal modes. It reads

$$A_{m,n}(\chi) = c_0\chi^{k_1/2}(1-\chi)^{k_2}, \text{ for } 0 \le \chi \le 1 \qquad (5.51)$$

and is zero elsewhere. As can be seen, this perturbation vanishes at the boundary, where χ=1. The parameters c_0, k_1 and k_2 are again fitted to the experimental MSE and ECE data. The radial derivative of the ideal perturbation is given by

$$\frac{\partial A_{m,n}(\chi)}{\partial \chi} = \frac{c_0 k_1}{2}\chi^{k_1/2-1}(1-\chi)^{k_2} - c_0 k_2 \chi^{k_1/2}(1-\chi)^{k_2-1}, \text{ for } 0 \le \chi \le 1 \qquad (5.52)$$

5.6 Alfvén eigenmodes

When a perturbation describing an Alfvén eigenmode is considered, the approximation of static perturbation isn't valid anymore. This is due to the high frequency of the perturbation, which has to be taken into account. The new model for the perturbation reads

$$\alpha(\chi,\theta,\zeta,t) = \sum_{n,m} A_{m,n}(\chi)\cos(m\theta - n\zeta - \omega t), \qquad (5.53)$$

where ω is the frequency of the eigenmode. It is, however, not enough to add a time dependence to the perturbation. The time dependence of the magnetic field

induces, as can be understood by the Maxwell's equations, an electric field. The electric field satisfies the condition $E_{\|} = 0$, which can be written in a more transparent form

$$0 = E_{\|} = -\nabla\tilde{\phi} - \frac{\partial}{\partial t}(\alpha B), \tag{5.54}$$

where B is the unperturbed magnetic field and $\tilde{\phi}$ is the perturbation in the electric potential. The time dependence also brings a new partial derivative to the equations of motion, i.e.

$$\frac{\partial \alpha}{\partial t} = \omega A_{m,n}(\chi)\sin(m\theta - n\zeta - \omega t). \tag{5.55}$$

The frequency of the perturbation can actually so high that the fast particles essentially interact with a phase-averaged perturbation. Hence, it could be possible in some cases to simulate AE with an effective parallel diffusion coefficient instead of a rotating perturbation. This is, however, not considered in this thesis.

5.7 Implementation in ASCOT code

The magnetic islands appear in ASCOT in the equations of motion, as was indicated in the previous Sections. At the moment, the island model can be used only when the magnetic coordinates are applied, even though a similar expression can be derived for the Cartesian equations of motion as well. The perturbative terms are calculated in a separate subroutine only when the MHD model is used. Hence, the magnetic background file is unaltered and can be used for simulation of several modes. The parameters for the radial perturbations are given in a general input file.

Chapter 6

Applications of magnetic island model

In this Chapter, two applications modelling magnetic islands are presented. In an axisymmetric magnetic field the fast ions are reasonably well confined. The reality, however, is far from the axisymmetric case. The limited number of toroidal field coils introduce a magnetic ripple, a periodic perturbation to the magnetic field strength in the toroidal direction. Moreover, instabilities such as magnetic islands break the assumption of axisymmetry. In a non-axisymmetric field, fast ions are subject to strong drift motions, i.e. they travel from one flux surface to another. This means that some of the fast ions escape the confinement and hit the PFC's. To be more precise, in the case of magnetic islands, the stationary island itself provides a channel to transport heat and particles radially. The main goal is, of course, to find out how these fast ion losses are minimized. After all, the fast ions should be kept inside the plasma for sufficient plasma heating and to spare the PFC's from excessive heat loads.

6.1 Validation of the implementation

To be sure that the mathematical model has been implemented correctly, the following tests were made:

- Islands should be evident when a particle field-line trace is made (Poincaré plot)

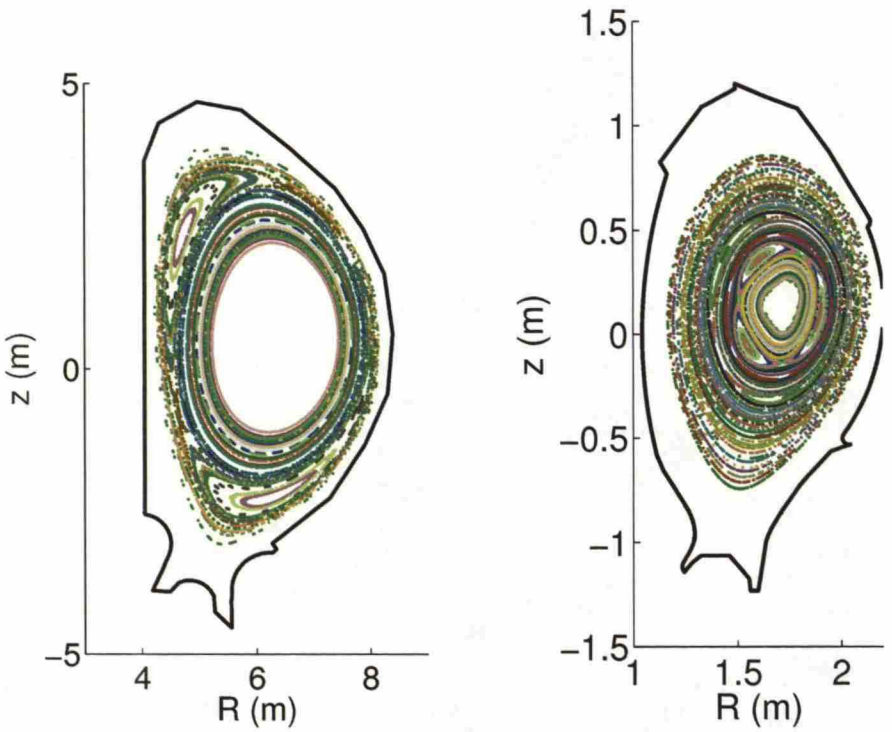

Figure 6.1: Magnetic islands in tokamaks. (a) A Poincaré plot of a (2,1) perturbation in ITER and (b) A Poincaré plot of a (3,2) and (2,1) perturbation with a constant radial profile in ASDEX Upgrade.

- A deformation of the flux surfaces near the core should appear when the perturbation is modeled without a radial profile
- The island width should be proportional to the square root of the perturbation amplitude
- Overlapping islands should form a stochastic magnetic field in the overlapping region.

The particle field line tracing is made in the following manner. Slow ions (with less than thermal energy) are launched parallel to the local magnetic field. Hence, the drifts are minimized and the velocity parallel to the magnetic field

will make sure that these particles follow very accurately magnetic field lines as can be seen from Eq. (2.25). When these ions pass through a certain toroidal angle, the (R, z) position of the particle is recorded. As a result, a poloidal cross section of magnetic flux tubes is obtained. When a perturbation to the magnetic field is introduced, these tubes break down and an island-like structure appears, as illustrated in Fig. 6.1(a). As can be seen from Eq. (2.12), the unperturbed flux goes to zero at the core. Should a constant radial perturbation be used, being non-zero at the core it creates an artificial island-like structure to the flux tubes at the core. This is shown in Fig. 6.1(b).

The island width is theoretically shown [15] to be proportional to the square root of the perturbation strength. To validate the ASCOT implementation, this was checked by drawing Poincaré plots for different perturbation strengths and visually reading the island width from the plot. The result, shown in Fig. 6.2, is very close to a straight line. Taking into account that the island width was measured by rather inaccurate means, the result is satisfactory. Last but not least, two overlapping islands were observed to produce a stochastic magnetic field in the region were the islands overlapped. Hence, the implementation was verified to produce physical results.

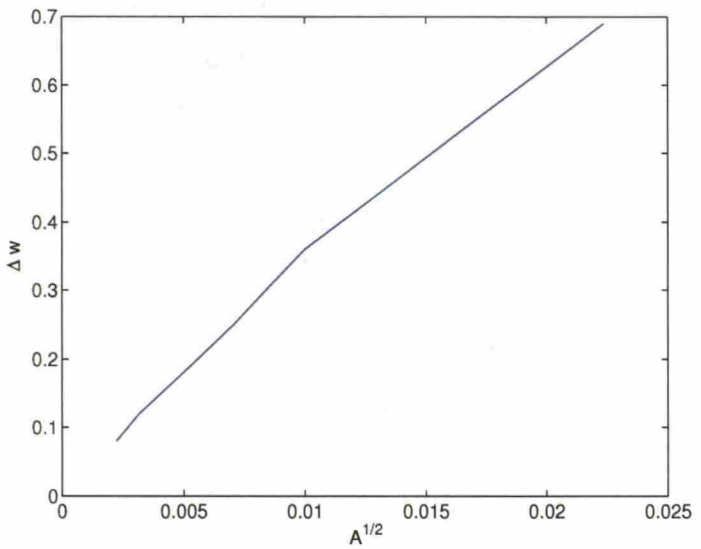

Figure 6.2: The island width as a function of the square root of the perturbation strength.

6.2 Fast ion losses due to NTM's

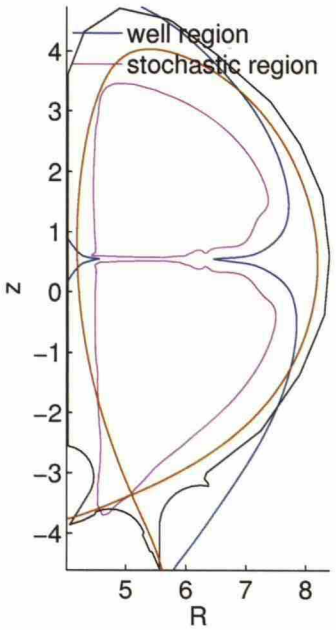

Figure 6.3: Regions of two different ripple-induced loss mechanisms in ITER.

Fast ions are lost due to the delicate interplay between the ripple and the magnetic islands, NTM's in this thesis. A lot of work has been dedicated to studying the ripple losses and the NTM-induced losses separately [24, 46, 57–59]. Less attention has been paid to the fact that these two are not separate effects. The ripple losses were already studied in Section 4.2 and here they are reintroduced in order to understand the above-mentioned interplay. The ripple affects the transport in two different ways. First, the deeply trapped orbits will be trapped to the ripple well caused by the toroidal gradient of the magnetic field strength. After being trapped in a ripple well, the particles escape confinement due to the gradient drift, i.e. Eq. 2.20 introduced in Section 2.3. Second, the ripple will alter the orbits of other particles, mainly banana orbits, leading to perpendicular transport. This process is often called stochastic diffusion. There are many channels for particles to enter the well region, e.g. by pitch and energy collisions. When the NBI beam makes a large angle with the magnetic field (a so-called near-perpendicular beam), the fast particles may be ionized in the

well region, and a significant portion of the beam energy may be lost through the ripple well transport mechanism. One important channel to the ripple well region are MHD instabilities such as NTM's. The resonance surface of the instability can be safely inside the separatrix, but it might extend to the ripple well region, which is enough to transport a large portion of fast particles rapidly out of the plasma.

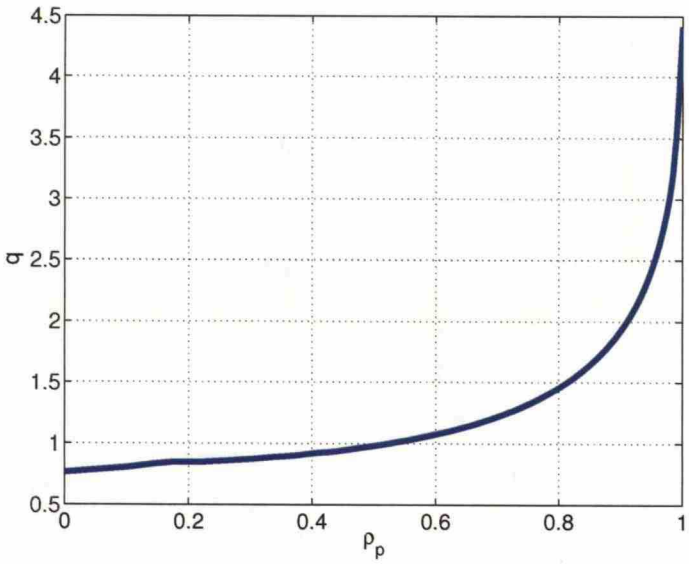

Figure 6.4: The safety factor q_s of ITER scenario 2 vs. radial coordinate ρ_p. The q=3/2 resonance surface is situated rather deep in the plasma, while the q=2/1 resonance surface is very close to the separatrix.

In this Section, we present preliminary results for the effect of static magnetic islands on the fast ion losses in an axisymmetric field. The interplay is not studied here, as it requires a ripple model in the magnetic coordinates, which was not available at the time. Three different cases were studied. The first, from now on Case 1, is a standard ASCOT run without any field perturbations. This was done for comparison. The second one, Case 2, was a (3,2) NTM discharge. The island width was adjusted to be 10 cm at the outer midplane, which is the critical size for mode locking of the (2,1) island according to [60]. The resonance surface is deep in the plasma, which can be seen from Fig. 6.4, and, hence, without the ripple effects, the α-particle wall load distribution should resemble the one obtained from Case 1. The last case, Case 3, is a (2,1) NTM

discharge with the resonance surface just inside the separatrix, as shown in Fig. 6.4. Hence, even without the ripple channeling, a clear difference in the wall loads due to NTM activity is expected. Due to the fact that the magnetic flux surfaces are compressed near the separatrix, the spatial width of the islands is very small. However, the perturbation amplitude was the same as in Case 2. The same set of input files, including the magnetic background, were used throughout the study.

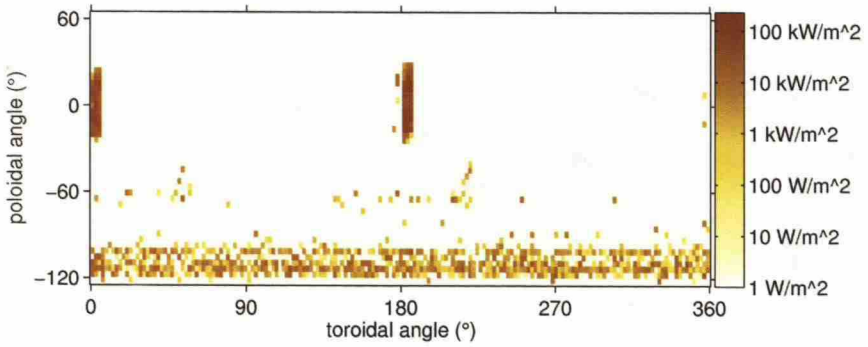

Figure 6.5: Wall load distribution in 2D for Case 1. Note the hot limiters and divertor plates. Cases 2 and 3 look very similar.

The 2D wall load for Case 1 is shown in Fig. 6.5. The hot limiters and divertor plates glow in red and yellow. Even though the wall distribution is slightly different in Cases 2 and 3, the differences in the 2D figures are too small to be readily seen. However, the differences are more easily seen in the ϕ-averaged wall loads shown in Fig. 6.6. Case 1 and 2 differ only in the limiter region, around θ=0, where the deep NTM slightly increases the wall load. On the other hand, the NTM at the edge, Case 3 shown in red, clearly increases the wall loads. This effect is even more severe when the ripple will be included in the simulation. Even the deep NTM of Case 2 might be enough to channel the particles to the ripple well region and, thus, increase to the wall load significantly.

6.3 Redistribution of fast ions due to the magnetic islands

One important issue in reactor-relevant tokamaks is steady state operation. Current tokamaks operate in pulses, which is unacceptable for a commercial reactor. The main problem in obtaining steady state operation with a reversed magnetic

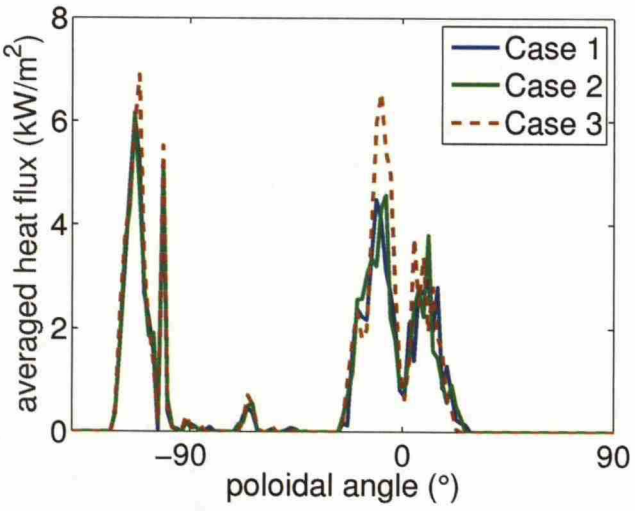

Figure 6.6: Comparison of the toroidally averaged wall load as a function of the poloidal angle. Blue: no perturbation. Green: NTM island deep in plasma. Red: NTM island near separatrix.

shear is driving the toroidal plasma current, which in pulsed operation is induced by the central transformer. The current can be driven by the neutral beam ions, electron cyclotron waves, lower hybrid waves or the plasma itself in the form of bootstrap current discussed below. Not only the total current but also the current profile is important in the sense that the current profile affects plasma confinement and provides resilience against MHD instabilities.

An especially important piece of the radial profile is off-axis current. It can be driven by, e.g., lower hybrid waves. Another key issue is the density and temperature gradient driven bootstrap current [61, 62]. By the present understanding, it can cover almost half of the total current needed for steady state operation. Thus, current drive plays a significant role in future tokamaks.

In NTM-rich plasmas, the NBI born fast ions used to drive the current may redistribute in an unwanted manner. This may lead to the loss of steady state operation as the current drive is centralized to the core, or passing particles are directed to trapped orbits by collisions. Knowledge of this kind of phenomena is critical to the successful steady state operation of ITER, and, hence, it should be studied in full detail. ASCOT serves as a perfect tool to perform relevant simulations on the slowing-down time scale, in the future it will be used to

obtain a deeper knowledge about the interplay between the magnetic islands and current drive.

Chapter 7

Discussion and future work

In this thesis, ASCOT was enhanced with two new simulation models. ASCOT can now take into account the finite Larmor radius of the fast ions by integrating the gyro motion of the particle. ASCOT can also simulate discharges with NTM activity. These two implementations have been validated and verified. Full orbit integration was used to simulate the wall load distributions due to fusion born α particles in ITER. As a conclusion, it was found that the finite Larmor radius effects are significant only in a strong ripple scenarios. With optimization against ripple, the difference between full orbit and guiding centre schemes was found to be negligible, thus justifying the use of guiding centre simulation. Full orbit integration was also applied to obtain more accurate wall load distributions with minimal CPU cost by using the guiding centre formalism until reaching the vicinity of the wall, backtracking the last integration step and repeating it by full orbit integration. The result was observed to differ notably from the typical way of recording the wall collisions by pure guiding centre simulation. More realistic wall load simulations have thus been made possible.

The model for magnetic islands was used to simulate wall load distributions of alpha particles in ITER in the presence of MHD modes. It was observed that the NTM activity near the edge of the plasma will increase the wall load even without magnetic ripple, while the deep-lying NTM will hardly differ from the non-perturbed case. In the near future, a more detailed study of the wall load distribution caused by the interplay of magnetic field ripple and NTM activity will be made. Furthermore, the magnetic island model will be applied to study the redistribution of fast ions and in particular current drive by neutral beam ions during NTM activity.

Acknowledgments

This work was partially funded by the Academy of Finland project No. 121371. The supercomputing resources of CSC - IT center for science were utilized in the studies. This work, supported by the European Communities under the contract of Association between Euratom/Tekes, was carried out within the framework of the European Fusion Development Agreement. The views and opinions expressed herein do not necessarily reflect those of the European Commission.

Bibliography

[1] M. O. Hagler and M. Kristiansen. *An introduction to controlled thermonuclear fusion*. Elsevier B.V., Lexington (MA), 1977. ISBN 0-669-99119-8.

[2] J. Sheffield. The physics of magnetic fusion reactors. Rev. Mod. Phys., 66(3) 1015–1103, 1994. doi:10.1103/RevModPhys.66.1015.

[3] D. Meade. 50 years of fusion research. Nuclear Fusion, 50(1) 014 004, 2010. doi:10.1088/0029-5515/50/1/014004.

[4] K. Ikeda. ITER on the road to fusion energy. Nuclear Fusion, 50(1) 014 002, 2010. doi:10.1088/0029-5515/50/1/014002.

[5] J. Jacquinot. Fifty years in fusion and the way forward. Nuclear Fusion, 50(1) 014 001, 2010. doi:10.1088/0029-5515/50/1/014001.

[6] T. Hauff, M. J. Pueschel, T. Dannert, and F. Jenko. Electrostatic and magnetic transport of energetic ions in turbulent plasmas. Physical Review Letters, 102(7):075004, 2009. doi:10.1103/PhysRevLett.102.075004.

[7] H. Mimata, K. Tani, K. Tobita et al. Finite Larmor radius effects on ripple diffusion in tokamaks. Progress in Nuclear Energy, 50(2-6) 638 – 642, 2008. ISSN 0149-1970. doi:10.1016/j.pnucene.2007.11.071.

[8] K. G. McClements. Full orbit computations of ripple-induced fusion alpha-particle losses from burning tokamak plasmas. Physics of Plasmas, 12(7):072510, 2005. doi:10.1063/1.1936532.

[9] K. G. McClements and A. Thyagaraja. Collisionless fast particle transport in tokamak plasmas with rotating magnetic islands. Plasma Physics and Controlled Fusion, 49(9) 1415, 2007. doi:10.1088/0741-3335/49/9/005.

[10] H. Zohm, G. Gantenbein, A. Gude et al. The physics of neoclassical tearing modes and their stabilization by ECCD in ASDEX Upgrade. Nuclear Fusion, 41(2) 197, 2001. doi:10.1088/0029-5515/41/2/306.

[11] S. Günter, G. Gantenbein, A. Gude et al. Neoclassical tearing modes on ASDEX Upgrade: improved scaling laws, high confinement at high β N

and new stabilization experiments. Nuclear Fusion, 43(3) 161, 2003. doi: 10.1088/0029-5515/43/3/301.

[12] H. Alfvén. Existence of Electromagnetic-Hydrodynamic Waves. Nature, 150 405–406, 1942. doi:10.1038/150405d0.

[13] L. Chen. Alfvén waves: a journey between space and fusion plasmas. Plasma Physics and Controlled Fusion, 50(12) 124 001, 2008. doi: 10.1088/0741-3335/50/12/124001.

[14] F. Waelbroeck. Theory and observations of magnetic islands. Nuclear Fusion, 49(10) 104 025, 2009. doi:10.1088/0029-5515/49/10/104025.

[15] J. Wesson. *Tokamaks*, volume 48 of *The Oxford Engineering Science Series*. Clarendon Press, 2nd edition, 1997. ISBN 0-19-856293-4.

[16] F. F. Chen. *Introduction to plasma physics*. Plenum Press, New York, 1 edition, 1974.

[17] K. A. Brueckner. *Inertial confinement fusion*. AIP, New York, 1992. ISBN 0-88318-925-9 (sid.).

[18] M. Wakatani. *Stellarator and heliotron devices*. Oxford University Press, New York, 1998. ISBN 0-19-507831-4.

[19] K. S. Krane. *Introductory nuclear physics*. Wiley, New York, 1988. ISBN 0-471-85914-1 (nid.).

[20] D. J. Griffiths. *Introduction to quantum mechanics*. Pearson Prentice Hall, Upper Saddle River, NJ, cop. 2005. ISBN 0-13-111892-7 (inb.).

[21] G. Federici, R. A. Anderl, P. Andrew et al. In-vessel tritium retention and removal in ITER. Journal of Nuclear Materials, 266-269 14 – 29, 1999. ISSN 0022-3115. doi:10.1016/S0022-3115(98)00876-9.

[22] P. C. Stangeby. *The plasma boundary of magnetic fusion devices*. Institute of Physics, Bristol, cop. 2000. ISBN 0-7503-0559-2.

[23] M. Bacal. Physics aspects of negative ion sources. Nuclear Fusion, 46(6) S250, 2006. doi:10.1088/0029-5515/46/6/S05.

[24] T. Kurki-Suonio, O. Asunta, T. Hellsten et al. ASCOT simulations of fast ion power loads to the plasma-facing components in ITER. Nuclear Fusion, 49(9) 095 001, 2009. doi:10.1088/0029-5515/49/9/095001.

[25] G. Kuo-Petravic, A. H. Boozer, J. A. Rome, and R. H. Fowler. Numerical evaluation of magnetic coordinates for particle transport studies in asymmetric plasmas. Journal of Computational Physics, 51(2) 261 – 272, 1983. ISSN 0021-9991. doi:10.1016/0021-9991(83)90092-X.

[26] R. L. Dewar, D. A. Monticello, and W. N.-C. Sy. Magnetic coordinates for equilibria with a continuous symmetry. Physics of Fluids, 27(7) 1723–1732, 1984. doi:10.1063/1.864828.

[27] A. H. Boozer. Plasma equilibrium with rational magnetic surfaces. Physics of Fluids, 24(11) 1999–2003, 1981. doi:10.1063/1.863297.

[28] A. H. Boozer. Time-dependent drift Hamiltonian. Physics of Fluids, 27(10) 2441–2445, 1984. doi:10.1063/1.864525.

[29] D. J. Griffiths. *Introduction to electrodynamics*. Prentice Hall, Upper Saddle River (NJ), 1999. ISBN 0-13-805326-X (sid.).

[30] T. G. Northrop. The guiding center approximation to charged particle motion. Annals of Physics, 15(1) 79 – 101, 1961. ISSN 0003-4916. doi: 10.1016/0003-4916(61)90167-1.

[31] X. Tao, A. A. Chan, and A. J. Brizard. Hamiltonian theory of adiabatic motion of relativistic charged particles. Physics of Plasmas, 14(9):092107, 2007. doi:10.1063/1.2773702.

[32] J. A. Heikkinen and S. K. Sipilä. Power transfer and current generation of fast ions with large-k_θ waves in tokamak plasmas. Physics of Plasmas, 2(10) 3724–3733, 1995. doi:10.1063/1.871072.

[33] O. Asunta. Personal communication, 2010.

[34] A. H. Boozer and G. Kuo-Petravic. Monte Carlo evaluation of transport coefficients. Physics of Fluids, 24(5) 851–859, 1981. doi:10.1063/1.863445. ASCOT collision operator ref.

[35] S. Sipilä and J. Heikkinen. ASCOT: Accelerated Simulation of Charged Particle Orbits in a Tokamak. Report TKK-F-A698, Helsinki University of Technology, 1992.

[36] M. N. Rosenbluth, R. D. Hazeltine, and F. L. Hinton. Plasma Transport in Toroidal Confinement Systems. Physics of Fluids, 15(1) 116–140, 1972. doi:10.1063/1.1693728.

[37] J. Heikkinen, S. Karttunen, T. Pättikangas, and S. Sipilä. Runaway losses in current ramp-up with lower hybrid waves. Nuclear Fusion, 33(6) 887, 1993. doi:10.1088/0029-5515/33/6/I05.

[38] J. Heikkinen and S. Sipilä. Monte Carlo simulation of minority ion bootstrap current by off-axis ion cyclotron heating in tokamaks. Nuclear Fusion, 37(6) 835, 1997. doi:10.1088/0029-5515/37/6/I10.

[39] J. A. Heikkinen, T. P. Kiviniemi, and A. G. Peeters. Neoclassical Radial Current Balance in Tokamaks and Transition to the *H* Mode. Phys. Rev. Lett., 84(3) 487–490, 2000. doi:10.1103/PhysRevLett.84.487.

[40] T. Kurki-Suonio, T. Kiviniemi, S. Sipilä et al. Monte Carlo simulations of the heat load asymmetries on JET divertor plates. Nuclear Fusion, 42(6) 725, 2002. doi:10.1088/0029-5515/42/6/310.

[41] H. X. Vu and J. U. Brackbill. Accurate numerical solution of charged particle motion in a magnetic field. J. Comput. Phys., 116(2) 384–387, 1995. ISSN 0021-9991. doi:10.1006/jcph.1995.1037.

[42] T. Tajima. *Computational plasma physics: with applications to fusion and astrophysics.* Addison-Wesley, Redwood City (CA) :, 1989. ISBN 0-201-16411-6.

[43] D. Tskhakaya, K. Matyash, R. Schneider, and F. Taccogna. The Particle-In-Cell Method. Contributions to Plasma Physics, 47(8-9) 563–594, 2007. ISSN 1521-3986. doi:10.1002/ctpp.200710072.

[44] M. Shimada, D. Campbell, V. Mukhovatov et al. Chapter 1: Overview and summary. Nuclear Fusion, 47(6) S1, 2007. doi:10.1088/0029-5515/47/6/S01.

[45] R. Hawryluk, D. Campbell, G. Janeschitz et al. Principal physics developments evaluated in the ITER design review. Nuclear Fusion, 49(6) 065 012, 2009. doi:10.1088/0029-5515/49/6/065012.

[46] K. Shinohara, T. Oikawa, H. Urano et al. Effects of ferromagnetic components on energetic ion confinement in ITER. Fusion Engineering and Design, 84(1) 24 – 32, 2009. ISSN 0920-3796. doi:10.1016/j.fusengdes.2008.08.040.

[47] S. Putvinski. Physics of energetic particles in ITER. Nuclear Fusion, 38(9) 1275, 1998. doi:10.1088/0029-5515/38/9/302.

[48] K. Tobita, T. Nakayama, S. V. Konovalov, and M. Sato. Reduction of energetic particle loss by ferritic steel inserts in ITER. Plasma Physics and Controlled Fusion, 45(2) 133, 2003. doi:10.1088/0741-3335/45/2/305.

[49] F. I. Parra and P. J. Catto. Limitations of gyrokinetics on transport time scales. Plasma Physics and Controlled Fusion, 50(6) 065 014, 2008. doi:10.1088/0741-3335/50/6/065014.

[50] W. M. Manheimer and C. N. Lashmore-Davies. *MHD and Microinstabilities in Confined Plasma.* Adam Hilger, Bristol, 1989. ISBN 0-85274-282-7.

[51] J. P. Freidberg. *Ideal Magnetohydrodynamics*. Plenum Press, New York, 1987. ISBN 0-306-42512-2.

[52] M. Schittenhelm and H. Zohm. Analysis of coupled MHD modes with Mirnov probes in ASDEX Upgrade. Nuclear Fusion, 37(9) 1255, 1997. doi:10.1088/0029-5515/37/9/I06.

[53] A. H. Boozer. Guiding center drift equations. Physics of Fluids, 23(5) 904–908, 1980. doi:10.1063/1.863080.

[54] R. B. White. *The theory of toroidally confined plasmas*. Imperial College Press, London, 2001. ISBN 1-86094-277-6.

[55] R. B. White and M. S. Chance. Hamiltonian guiding center drift orbit calculation for plasmas of arbitrary cross section. Physics of Fluids, 27(10) 2455–2467, 1984. doi:10.1063/1.864527.

[56] S. Pinches, L. Appel, J. Candy et al. The HAGIS self-consistent non-linear wave-particle interaction model. Computer Physics Communications, 111(1-3) 133 – 149, 1998. ISSN 0010-4655. doi:10.1016/S0010-4655(98)00034-4.

[57] V. Hynönen, T. Kurki-Suonio, W. Suttrop, A. Stäbler, and the ASDEX Upgrade Team. Effect of radial electric field and ripple on edge neutral beam ion distribution in ASDEX Upgrade. Plasma Physics and Controlled Fusion, 50(3) 035 014 (15pp), 2008. doi:10.1088/0741-3335/50/3/035014.

[58] E. Strumberger, S. Günter, E. Schwarz, C. Tichmann, and the ASDEX Upgrade Team. Fast particle losses due to NTMs and magnetic field ripple. New Journal of Physics, 10(2) 023 017 (21pp), 2008. doi:10.1088/1367-2630/10/2/023017.

[59] M. Gobbin, L. Marrelli, H. Fahrbach et al. Numerical simulations of fast ion loss measurements induced by magnetic islands in the ASDEX Upgrade tokamak. Nuclear Fusion, 49(9) 095 021, 2009. doi:10.1088/0029-5515/49/9/095021.

[60] R. L. Haye, A. Isayama, and M. Maraschek. Prospects for stabilization of neoclassical tearing modes by electron cyclotron current drive in ITER. Nuclear Fusion, 49(4) 045 005, 2009. doi:10.1088/0029-5515/49/4/045005.

[61] C. Kessel. Bootstrap current in a tokamak. Nuclear Fusion, 34(9) 1221, 1994. doi:10.1088/0029-5515/34/9/I04.

[62] W. A. Houlberg, K. C. Shaing, S. P. Hirshman, and M. C. Zarnstorff. Bootstrap current and neoclassical transport in tokamaks of arbitrary collisionality and aspect ratio. Physics of Plasmas, 4(9) 3230–3242, 1997. doi: 10.1063/1.872465.